SUBSTRATE ENTRAINMENT, DEPOSITIONAL RELIEF, AND SEDIMENT CAPTURE: IMPACT OF A SUBMARINE LANDSLIDE ON FLOW PROCESS AND SEDIMENT SUPPLY

Authors:

Martínez-Doñate, A.[1], *Privat, A.[2], Hodgson, D.M.[2], Jackson, C.A-L.[1], Kane, I.A.[1], Spychala, Y. T. [3], Duller, R.A.[4], Stevenson, C.[4], Keavney, E. [2], Schwarz, E.[5], Flint, S.S.[1]*

- *School of Earth and Environmental Sciences, University of Manchester, Manchester M13 9PL, UK.*
- *School of Earth and Environment, University of Leeds, Leeds LS29JT, UK.*
- *Institute for Geology, Leibniz University Hannover, Callinstraße 30, Hannover 30167, Germany*
- *Department on Earth, Ocean, and Ecological Sciences, University of Liverpool, 4 Brownlow Street, Liverpool L69 3GP, UK*
- *Centro de Investigaciones Geológicas (CIG), La Plata, Provincia de Buenos Aires, Argentina*

Corresponding author: ander.martinez-donate@manchester.ac.uk

ABSTRACT:

Submarine landslides can generate complicated patterns of seafloor relief that influence subsequent flow behaviour and sediment dispersal patterns. While the large-scale morphology of submarine landslide deposits, or mass transport deposits (MTDs), can be resolved in seismic data, the nature of their upper surface, and its impact on facies distributions and stratal architecture of overlying deposits, is rarely resolvable. MTD is a commonly used term in

subsurface studies, covering a range of processes and resultant deposits that can not be resolved in seismic or core-based datasets. However, field-based studies often allow a more detailed characterisation of the deposit. The early post-rift Middle Jurassic deep-water succession of the Los Molles Formation is exceptionally well-exposed along a dip-orientated WSW-ENE outcrop belt in the Chacay Melehue depocentre, Neuquén Basin, Argentina. We correlate 27 sedimentary logs constrained by marker beds to document the sedimentology and architecture of a >47 m thick and at least 9.6 km long mud-rich debrite. The debrite overlies ramps and steps, indicating erosion and substrate entrainment. Megaclasts sourced from shallow-marine environments support a shallow marine origin of the mass failure. Two distinct sandstone-dominated units overlie the debrite. The lower sandstone unit is characterised by: i) abrupt thickness changes, wedging and progressive rotation of laminae in sandstone beds associated with growth strata; and ii) detached sandstone load balls within the underlying debrite. The combination of these features suggests syn-sedimentary foundering processes due to density instabilities at the top of the fluid-saturated mud-rich debrite. The debrite relief controlled the spatial distribution of foundered sandstones. The upper sandstone unit is characterised by thin-bedded deposits, locally overlain by medium- to thick-bedded lobe axis/off-axis deposits. The thin-beds show local thinning and onlapping onto the debrite, where it develops its highest relief. Facies distributions and stacking patterns record the progradation of submarine lobes and their complex interaction with long-lived debrite-related topography. These characteristics can help us understand post-depositional processes above MTDs and predict facies distributions and palaeoenvironments in subsurface datasets. The emplacement of a kilometre-scale debrite in an otherwise mud-rich basinal setting and accumulation of overlying sand-rich deposits suggests a genetic link between the mass-wasting event and transient coarse clastic sediment supply to an otherwise sand-starved part of the basin.

Keywords: Submarine Landslide, Submarine lobe, Foundering, Dynamic topography, Relief, Confinement, Neuquén Basin.

INTRODUCTION

Submarine landslide deposits, or Mass Transport Deposits (MTDs) (Nardin *et al.*, 1979), are sedimentary bodies that have been translated downslope from high to low gradient slopes as a result of mass failure and gravitational processes (Hampton *et al.*, 1995; Moscardelli & Wood, 2008; Kneller *et al.*, 2016). The typically cohesive nature of the flows enables the transportation of megaclasts (McGilvery & Cook, 2003; Lee *et al.*, 2004; Jackson, 2011; Hodgson *et al.*, 2019; Nwoko *et al.*, 2020a). Megaclasts within MTDs are sourced either from headwall areas or entrained from the substrate. These features, accompanied by syn- and post-depositional faulting (Dykstra, 2005; Dykstra *et al.*, 2011), generate the topographically irregular upper surfaces of MTDs (Moscardelli *et al.*, 2006; Bull *et al.*, 2009). Deep-water sediment gravity flows interact with the rugose topography of MTDs, which influences flow behaviour, deceleration and steadiness (Lowe & Guy, 2000; Armitage *et al.*, 2009; Jackson & Johnson, 2009; Fairweather, 2014; Ortiz-Karpf *et al.*, 2015, 2017; Steventon *et al.*, 2021), and therefore dispersal patterns and depositional architecture (Kneller *et al.*, 2016). MTD surface relief has been shown to affect facies distribution and associated sedimentary architecture; this has been reported from both outcrop (Pickering & Corregidor, 2005; Armitage *et al.*, 2009; Dykstra *et al.*, 2011; Fallgatter *et al.*, 2017; Brooks *et al.*, 2018; Valdez *et al.*, 2019) and subsurface studies (Ortiz-Karpf *et al.*, 2017; Nwoko *et al.*, 2020b). However, MTDs may continue to deform after initial emplacement through creeping processes (e.g. Butler & McCaffrey, 2010) or secondary mass movements (Sobiesiak *et al.*, 2016). Furthermore, the high water content within newly deposited MTDs promotes active dewatering at their upper surface (Mulder & Alexander, 2001; Talling *et al.*, 2012; Browne *et al.*, 2020) associated with local instabilities and

movement (Iverson, 1997; Major & Iverson, 1999; Van der Merwe *et al.*, 2009). Fluids can also generate overpressure along with the interface between MTDs and its sediment cover, exploiting pathways created by internal MTD deformation (Migeon *et al.*, 2014; Praeg *et al.*, 2014). Therefore, the interaction between the initial topographic relief of MTDs, dewatering processes, post-depositional deformation and subsequent sediment gravity flows (and their deposits) is highly dynamic and inherently complex (e.g. Alves, 2015). MTD is a commonly used term in subsurface studies, covering a range of processes and resultant deposits that can not be resolved in seismic or core-based datasets. However, field-based studies often allow a more detailed characterisation of the deposit.

Here, we aim to understand an exceptionally well-exposed debrite and overlying sand-rich strata in the Bathonian Los Molles Formation, which were physically correlated over 9.6 km along a depositional dip transect in the Chacay Melehue depocenter (Neuquén Basin, Argentina). The objectives of this study are to i) document the anatomy and stratigraphic architecture of the debrite, ii) investigate the impact of the dynamic upper relief on the overlying heterolithic and sand-rich strata, and iii) discuss the role that mass-wasting processes may have played as a trigger for subsequent sand-rich sediment supply.

GEOLOGICAL SETTING

The Neuquén Basin is located in central-western Argentina and central-eastern Chile, covering an area of 160,000 km^2 (Fig. 1A). The basin is bounded to the north-east by the Sierra Pintada, to the south by the North Patagonian Massif, and since the Early Jurassic, by the early Andean magmatic arc to the west (Legarreta & Gulisano, 1989; Suárez & de la Cruz, 1997; Franzese & Spalletti, 2001; Howell *et al.*, 2005). The Neuquén Basin contains a >6 km-thick sedimentary succession that spans the Mesozoic to the late Cenozoic and records several unconformities related to tectonic phases (Vergani *et al.*, 1995; Legarreta & Uliana, 1996; Howell *et al.*, 2005).

Three key tectonic phases are recognised (Vergani *et al.*, 1995; Franzese & Spalletti, 2001; Franzese *et al.*, 2003): i) Triassic-to-Early Jurassic rifting and the onset of subsidence; ii) Early Jurassic-to-Early Cretaceous post-rift thermal subsidence associated with the development of the Andean magmatic arc and back-arc basin; and iii) Late Cretaceous-to-Early Cenozoic Andean compression and foreland basin development. In the western sector of the Central Neuquén Basin, the deep- to shallow-marine deposits of the early post-rift Cuyo Group (Lower-to-Middle Jurassic) (Gulisano *et al.*, 1984) unconformably overlie the continental syn-rift volcano-sedimentary deposits of the Precuyano Group (Gulisano *et al.*, 1984; Gulisano & Gutiérrez Pleimling, 1995; Legarreta & Uliana, 1996; Pángaro *et al.*, 2009; Leanza *et al.*, 2013) or the Palaeozoic basement of the Choiyoi Group (Llambías *et al.*, 2003, 2007) (Fig. 2A).

Our investigation focuses on the Early Bathonian stratigraphy of the Upper Los Molles Formation, which forms a ~70 m thick interval characterised by ammonite-rich black shales and heterolithic successions comprising tuff layers with intervening MTD and sandstone deposits (Fig. 1B).

Study area - Chacay Melehue depocentre

The succession in the Chacay Melehue area was deposited in a half-graben (Manceda & Figueroa, 1995; Llambías *et al.*, 2007; Leanza *et al.*, 2013) that occupied the western and deepest part of a broader early post-rift depocentre in the Central Neuquén Basin (Manceda & Figueroa, 1995; Veiga *et al.*, 2013). The half-graben shows a strong asymmetry due to a steep western margin characterised by the development of the early Andean magmatic arc and location of a major syn-rift fault (Manceda & Figueroa, 1995; Suárez & de la Cruz, 1997; Vicente, 2005), which contrasts with the stable and gently dipping eastern cratonic margin (Spalletti *et al.*, 2012; Veiga *et al.*, 2013). Deposition of the Los Molles Formation took place during a period of thermal subsidence and regional transgression across complex inherited rift

topography, which promoted the reduction of sediment supply and sand starvation in this part of the basin (Spalletti *et al.*, 2012; Veiga *et al.*, 2013). The proximity to the volcanic arc (~30 km to the west), the abundant volcaniclastic deposits (Zöllner & Amos, 1973; Rosenfeld & Volldaeimer, 1980; Gulisano & Gutiérrez Pleimling, 1995; Suárez & de la Cruz, 1997; Vicente, 2005; Llambías *et al.*, 2007), and palaeocurrent measurements in sandstones indicating south-eastwards trend reveals that sediment supply feeding the Chacay Melehue area during the post-rift was sourced from the western magmatic arc. The deep-marine deposits of Los Molles Formation (Weaver, 1931) overlie shallow-marine tuffaceous clastic deposits (La Primavera Formation, Suárez & de la Cruz, 1997; Llambías & Leanza, 2005) and carbonate deposits of the Chachil Formation (Pliensbachian to Early Toarcian, Weaver, 1942; Kamo & Riccardi, 2009; Leanza *et al.*, 2013; Riccardi & Kamo, 2014), deposited with the first marine incursion in the basin (Gulisano & Gutiérrez Pleimling, 1995; Leanza *et al.*, 2013) (Fig. 2A). Chronostratigraphic studies based on ammonite biostratigraphy (Gulisano & Gutiérrez Pleimling, 1995; Riccardi, 2008) and U-Pb radiometric dating (Kamo & Riccardi, 2009; Leanza *et al.*, 2013; Riccardi & Kamo, 2014), place the Los Molles Formation in the Chacay Melehue region as Early Toarcian-to-Early Callovian in age (Gulisano & Gutiérrez Pleimling, 1995) (Fig. 2C). The succession of the Los Molles Formation in the Chacay Melehue depocentre is 850 m thick (Fig. 2B). A 55 m thick sandstone-prone interval in the lower succession represents an Aalenian turbidite system (interval II of Gulisano & Gutiérrez Pleimling, 1995). The overlying Bathonian section of the Los Molles Formation (up to 200 m thick) (Fig. 2B) is mainly represented by mudstone and heterolithic successions, including a 70 m thick interval (study interval; Fig 2C) of deformed sand- and mud-rich deposits (interval IV of Gulisano & Gutiérrez Pleimling, 1995). The overlying Lower Callovian strata of the Los Molles Formation is characterised by a 300 m thick interval of thin-bedded mudstone. It is overlain by either the fluvial Lotena Formation (Gulisano & Gutiérrez Pleimling, 1995; Veiga

156 *et al.*, 2011) or evaporites (Tábanos Formation; Fig. 2D), which record a period of basin
157 desiccation (Legarreta, 1991; Gulisano & Gutiérrez Pleimling, 1995; Legarreta & Uliana,
158 1996).
159
160 **METHODOLOGY**
161 The sedimentology and stratigraphic architecture of a 70 m thick interval (Figs. 2C and 3)
162 within the Upper Los Molles Formation were investigated along a 9.6 km long and WSW-ENE
163 orientated outcrop belt (Figs. 1B and 1C). The succession dips 10-20° to the SE, with minimal
164 structural overprint from the later tectonic inversion. Twenty-seven sedimentary logs were
165 measured at 1:25 to 1:40 scale along this transect (CML-0 to CML-27 from SW to NE) to
166 document the broad depositional architecture of 4 different units (Unit 1, 2, 3, 4A and B) (Fig.
167 1C). Ten detailed logs were measured at a 1:2 scale at specific locations to document fine-scale
168 thickness and facies changes. Four marker beds were used to build a robust physical correlation
169 between sedimentary logs (Figs. 2 and 3). The marker beds are i) Datum A, or the 'Burro'
170 marker bed, a light-grey indurated graded siltstone at the base of the study interval (Figs. 2A,
171 3 and 4A); ii) a gravelly thin-bed (Fig. 4F) and iii) a tuff layer (Fig. 4G), both within one of the
172 studied units (Unit 4A); and iv) Datum B, a tuff layer overlying the study interval (100-150 m
173 above) across the study area (Figs. 2D and 3). Uncrewed Aerial Vehicle (UAV)
174 photogrammetry (Figs. 2D and 5) was used in conjunction with standard field techniques to
175 capture the micro- and macro-scale features of the investigated stratigraphic units. Fifty-eight
176 palaeocurrent measurements were collected, consisting of ripples, cross-bedding, flame
177 structure and convolute lamination vergence, plotted in rose diagrams (Fig. 8).
178

SEDIMENTOLOGY AND STRATIGRAPHY

The study interval is subdivided informally into four different units (Fig. 2C), based on their distinctive facies and stratal relationships.

Unit 1

Description: Unit 1 is 5.5-28 m thick and contains the Burro marker bed (Datum A) (Fig. 2C), a light-grey indurated graded siltstone that is sharply overlain by light-grey fine-grained, planar-parallel laminated sandstone (Fig. 4A). This unit is truncated by the basal surface of Unit 2 and is thinnest in the central sector of the exposure (see sections CML-9 to CML-16 Fig. 3). Unit 1 comprises a heterolithic succession of planar-parallel laminated mudstones (F1) and thin-bedded (<0.1 m thick) normally-graded, well-sorted siltstones (F2) to very fine-grained sandstones (F3), and occasional medium-bedded structureless sandstones (F5) (Figs. 4A and 4C). When traced from west to east, the thin-bedded sandstones show subtle lateral fining and thinning, transitioning from heterolithic succession to mudstone-prone succession. Unit 1 is rich in ammonites, belemnite rostrums and bivalves, as well as calcareous concretions (Damborenea, 1990; Gulisano & Gutiérrez Pleimling, 1995; Riccardi *et al.*, 2011).

The central and eastern sectors contain a discrete stratigraphic interval that exhibits deformed bedding (Fig. 4B). This interval is thickest (at least 10 m; Fig. 3) in the central sector, where, internally, it exhibits an array of imbricated decametre-scale east-verging thrusts (offset < 2 m) and associated drag folds. The thrusts originate from a bed parallel surface, leaving the underlying bedding undeformed (Fig. 4B). In the eastern sector, a thin (~5 m thick) interval of intense deformation is characterised by open folds and minor thrusts (offset < 1 m) (Fig 4B). Unit 1 stratigraphy in the western sector lacks any deformation.

Interpretation: The laminated mudstones, graded siltstones and thin sandstone beds are interpreted as deposits of low-density turbidity currents (Allen, 1982; Trabucho-Alexandre *et*

al., 2012; Könitzer *et al.*, 2014), whereas the medium-bedded sandstones represent the deposits of medium- to high-density turbidity currents (Talling *et al.*, 2012). The laterally extensive character, mudstone dominance, and overall eastward (downdip) fining and thinning trend of thin-bedded sandstones of Unit 1 suggest deposition from low-energy sediment gravity flows in distal areas (e.g. Mutti, 1977), with possible distal lobe fringe deposits (Boulesteix *et al.*, 2020). The discrete intervals of deformed bedding found in the upper parts of Unit 1 represent a post-depositional sheared zone linked to the overlying Unit 2.

Unit 2

Description: Unit 2 has an erosive basal contact that truncates Unit 1 in the central sector (Fig. 3). The relief of the basal contact is characterised by down- and up-stepping segments (ramps, >2°) linked by bedding-parallel segments (flats). The average thickness of Unit 2 is 20-30 m but can locally reach up to > 47m in the central sector and abruptly thins to <8 m towards the eastern and western sectors (Fig. 3). This change in thickness coincides with deeper erosion on the basal surface. Unit 2 is characterised by a matrix-supported medium-grained muddy sandstone to sandy mudstone and is very poorly sorted throughout, ungraded, and with a chaotic distribution of outsized clasts (F14; Fig 4E). Clasts range in character and size from granular quartz grains and rounded volcanic epiclasts to much larger megaclasts (>4.1 - 140 m long) (Hodgson et al., 2019) of either conglomeratic or heterolithic lithology (Figs. 2C, 2D, 4C and 5). Typically, conglomeratic megaclasts are rounded, elongated and weakly deformed (Figs. 2D and 4C) and are clast-supported, with well-rounded to sub-angular clasts (0.03-1 m diameter) and fragments of thick-shelled bivalves (oysters; Fig. 4D). These oyster-bearing conglomeratic megaclasts are preferentially located near the base of Unit 2 (Figs. 2C, 2D and 3B). In contrast, heterolithic megaclasts are angular and characterised by internally folded packages of planar laminated and normally graded thin-bedded material (Figs. 2C and 5) and preferentially distributed toward the top of Unit 2 (Figs. 3 and 5).

Interpretation: The sedimentary characteristics of this unit suggest near-instantaneous deposition from a flow with high yield strength and buoyant support that could transport clasts up to 140 m long (Stow & Johansson, 2000; Mulder & Alexander, 2001). Using Datum A, the debrite formed a long-wavelength mounded top (Fig. 3), attributed to the parental flow's cohesive nature and en-masse freezing. We interpret Unit 2 as a cohesive debris flow deposit (Talling *et al.*, 2012). The ramp and flat geometry at the base of Unit 2 indicate the debris flow's erosive nature (e.g. Lucente & Pini, 2003).The similarity in composition between the heterolithic megaclasts and underlying Unit 1 suggests entrainment of deep-marine substrate blocks due to the shear stress exerted by the overriding debris flow (Hodgson *et al.*, 2019). In contrast, the oyster-bearing conglomerate megaclasts suggests a probable shallow marine shelf source. The two distinct megaclast sources suggest long-distance transport of clasts and flow bulking through local substrate entrainment (e.g. Sobiesiak *et al.*, 2016).

Unit 3

Description: Unit 3 (0-4 m thick) is composed of thick sandstone beds (0.5-2 m) with sharp, irregular concave-up bases and abrupt pinchout terminations, which result in a disconnected distribution of packages of wedge-shaped sandstone bodies (Fig. 6 (see architecture section). Unit 3 is only present where Unit 2 is relatively thin (in the eastern-central and western sectors) and is absent in the central region where Unit 2 shows its maximum thickness (Fig. 3). Where Unit 3 is absent, Unit 4 overlies Unit 2 (Figs. 3, 5 and 6). Unit 3 comprises bed types characterised by two main amalgamated divisions (lower and upper divisions) with some grain size breaks lacking any mudstone- and siltstone-rich bounding intervals (Figs. 6A and 7). The basal interface of these sandstone bodies shows centimetre-scale undulations characterised by

abundant load casts, semi-detached ball structures, and mudstone intrusions (diapirs) originating from Unit 2 (Fig. 6G).

Two different types of thick-bedded amalgamated sandstone facies dominate the lower division, which varies along the transect. Grain-size breaks define amalgams of sandstones. In the western sector, and more rarely in the eastern sector, the lower divisions are characterised by thick-bedded (0.5-2 m thick), structureless, weakly normally-graded, moderately- to poorly-sorted sandstones (F12). At bed bases, these sandstones comprise well-rounded (0.1-1 m diameter) mudstone clasts of low-sphericity and diffuse boundaries (mudstone clast type A), which show a coarse tail grading (Figs. 6A and 6G). Locally, in the eastern sector, lower divisions of these sandstone bodies comprise thick-bedded, structureless, very poorly-sorted, more argillaceous sandstones with abundant mudstone clasts (0.1 - 1 m diameter) with very diffuse boundaries (mudstone clast type A), which are ungraded and randomly orientated (F13) throughout the encasing matrix (Fig. 5F).

The lower division of Unit 3 sandstone bodies are overlain by an upper division (up to 2 m thick), which comprises coarse to very fine-grained, normally graded, moderately- to poorly-sorted sandstones (0.5-1.7 m) (Fig. 6A). Banding can be developed throughout the bed or overlying a structureless division (Fig. 6A). The banding is characterised by an alternation between lighter matrix-poor bands and darker matrix-rich bands that comprise bedding parallel millimetric mudstone clast with sharp boundaries (mudstone clast type B) (F8; Fig. 6C). Contacts between bands are diffuse (Fig. 6B and 6F). The spacing between the individual bands (0.5-2 cm) increases from the margin to central parts of the sandstone body (Fig. 8), commonly showing rotation (Fig. 6E). These sandstones develop symmetrical and asymmetrical convolute lamination at bed tops (predominant vergence towards NE; Fig. 6D). Decimetre-scale long and centimetre-scale thick mudstone injections can be observed within this division (Fig. 6B).

Interpretation: The wedge-shaped and deformed concave-up basal contacts of the sandstone bodies beds in Unit 3 are interpreted to reflect the interaction with the rugose upper surface and syn-sedimentary foundering of sand into the underlying mud-rich debrite (Figs. 6 and 9). Foundering is driven by instability due to the density contrast between the sand deposited above a less dense debrite (density loading) and lateral changes in sediment load (uneven loading) (Owen, 1987, 2003) produced by the short-wavelength rugosity of the upper surface.

The lack of sedimentary structures in the lower divisions of bed types recognised in Unit 3 is interpreted as a product of hindered settling from highly-concentrated gravity-flows, resulting in turbulence damping and rapid deposition (Talling *et al.*, 2012), inhibiting any period of traction (Sumner *et al.*, 2008). The normally-graded lower divisions were produced by incremental layer-by-layer deposition from high concentration gravity flows, such as high-density turbidity currents (sensu Lowe, 1982). In contrast, the thick-bedded argillaceous sandstones with ungraded mudstone clasts observed in the distal areas (eastern sector) are interpreted as moderate-strength cohesive debrites (sensu Talling *et al.*, 2012). The decimetre-scale mudstone clast (type A) was transported due to the matrix strength of the debris flows and their positive buoyancy with respect to the encasing matrix (Talling *et al.*, 2012).

The lateral facies transition from high-density turbidites to moderate strength cohesive debrite suggest a flow transformation due to the entrainment of cohesive material from the underlying debrite (e.g. Kane & Pontén, 2012; Baker *et al.*, 2017). The unconsolidated state of the debrite might have enhanced the substrate entrainment of decimetre-scale mudstone clasts (type A) and disaggregation (as indicated by the diffuse boundaries: Fig. 6G), increasing the amount of mud and, therefore, the cohesiveness of the flow. Based on facies juxtaposition, the foundered sandstones can be subdivided into two different facies associations: 1) proximal, and 2) distal, foundered sandstones facies associations (Fig. 7). Both high-density turbidites and moderate strength cohesive debrites are characterised by rapid deposition (incremental deposition and en

masse freezing, respectively), triggering the liquefaction of the fluid-saturated and unconsolidated upper surface of the debrite and foundering of sand (Fig. 9). The undulations of the concave-up basal interface reflect complex interactions with the substrate: as the denser sand sank into the fluid-saturated muddy substrate, the buoyancy of mud promoted the syn- to post-depositional intrusion (mud diapirs and injectites) of the substrate into sandstones. The most advanced stage of foundering is observed when detached sand-balls develop (Fig. 5; Owen, 2003; Tinterri *et al.*, 2016).

In contrast, the banded sandstones characteristic of the upper divisions are interpreted to be formed under either episodic near-bed turbulence damping (Lowe and Guy, 2000). The presence of diffuse boundaries suggests high rates of deposition (Lowe & Guy, 2000). The juxtaposition of the banded sandstones over the mudstone-clast bearing sandstones of the lower divisions suggests highly stratified flows, mixing and upwards transfer of centimetre-scale mudstone clast (type B) and the cohesive material from the disaggregation of the entrained decimeter-scale mudstone clast (type A). This enrichment in cohesive clayey material triggered the periodic suppression of turbulence and, therefore, banding development. The banding passes into convolute laminations towards the top, indicating moderate rates of deposition. The vergence of convoluted laminations suggests a syn-sedimentary shear-stress exerted by the overriding flow (McClelland *et al.*, 2011; Butler *et al.*, 2016) and flow-rebound produced by the underlying debrite relief (e.g. Tinterri *et al.*, 2016).

Unit 4

Description: Unit 4 (10-27.3 m thick) has a sharp and non-erosive contact with the underlying Unit 2 and Unit 3 (Fig. 3). It comprises two subunits: a lower heterolithic interval (Unit 4A) and an upper sandstone-prone interval (Unit 4B; Fig. 2C).

Unit 4A is thin- to medium-bedded (0.01-0.5 m; Fig 4H) heterolithic succession (F1, F2, F3 and F5) with a maximum thickness of 22 m, thinning to 8 m in the central sector above where Unit 2 is thickest (Fig. 3). Most of the thin-beds (0.01-0.1 m thick) are fine- to medium-grained normally-graded sandstones, matrix-poor, moderately well-sorted, and exhibit planar-parallel lamination and/or starved-ripple lamination (F3; Fig. 4C). Palaeocurrent measurement shows a consistent flow trend towards the NE (Fig. 9). Unit 4a also comprises coarse- to granular normal-graded sandstones (0.07-0.2 m thick) with erosive bases and sharp-planar tops (F4; Fig.4D) and two medium-bedded matrix-supported conglomerates with sandstone clasts (F14; 0.25 and 0.35 m thick, respectively) that pinch out towards the central sector (Fig. 8). One of these thin gravelly beds, which lacks any lateral thinning or fining trend (Fig. 4I) was traced across the exposure (gravelly marker bed; dashed red line in Fig. 8). In addition, a 0.15 m thick tuff layer (Fig. 4J) was also used for correlation purposes (tuff marker bed; dashed white line in Fig. 3). The medium-bedded sandstone (0.1–0.5 m thick) are structureless, ungraded, with planar-parallel and convolute lamination at bed tops, except one, which shows cross-bedding (F6; Fig.4D). These sandstones have sharp bed bases and tops and lack mudstone clasts. In the eastern sector, Unit 4A is dominated by thin- to medium-bedded heterolithic succession that lacks any gravelly (F5) or matrix-supported conglomerate beds (F14).

Unit 4B (5.7 m thick in the western sector) thins eastwards along a 4.3 km transect until it pinches out, where Unit 2 is thickest (Fig. 3). In the western sector, it dominantly comprises medium- (F5; Fig. 4K) to thick-bedded sandstones (F11; Fig. 4K), with less common "bipartite" sandstone beds (F9 and F10) composed of a matrix-poor lower division and a matrix-rich upper division with mudstone clasts. Non-erosive bases and sharp tops characterise the thick-bedded sandstones (0.5-1.2 m). Where the thick-bedded sandstones are not amalgamated and are intercalated centimetre-thick beds of fine-grained material (F1 and F2), bed bases are loaded locally. The thick-bedded sandstones are normally graded from medium

352 to fine sand, well-sorted with rare centimetric mudstone clasts at the bed top. Other soft-
353 sediment deformation structures, such as centimetre-scale flames with NE vergence, are also
354 common at bed bases and along amalgamation surfaces (Fig. 4L). Banded sandstones are
355 medium-bedded (0.1-0.5 m), fine- to medium-grained and characterised by an alternation
356 between light- and dark-coloured bands, ranging from 0.2 to 2 cm thick (F7; Fig. 4L). Both
357 band types show a similar maximum grain size, although the darker bands are matrix-rich, and
358 light bands are matrix-poor. Banding is generally sub-parallel to bedding. Although banded
359 sandstones are more commonly associated with thick-bedded structureless sandstones, the
360 banded sandstones can be individual event beds, with banding above the structureless basal
361 division. The medium-bedded bipartite sandstone beds (0.1-0.5 m) consist of a medium-
362 grained, matrix-poor and structureless lower division, which is overlain by a fine-grained
363 matrix-rich upper division characterised by poor sorting and abundant mudstone clasts (0.05-
364 0.3 m) with low sphericity and variable roundness (F9 and F10; Fig. 4M). The lower and upper
365 divisions show a gradual upwards increase in matrix content rather than across a sharp
366 boundary. When Unit 4B is traced eastwards towards the central sector, the sandstone package
367 transitions into a few thin-beds (0.1 m thick) of weakly graded, very poorly-sorted matrix-rich
368 sandstone, lacking the mudstone clasts observed in western areas. Unit 4B is absent in the
369 eastern sector.
370
371 Interpretation: In Unit 4A, the thin sandstone beds showing planar-parallel and cross ripple
372 laminations support an interpretation as low- to medium-density turbidites (Talling *et al.*,
373 2012). The starved-ripple lamination observed in thin-bedded sandstones is interpreted as the
374 reworking of sand deposited by dilute flows with low sedimentation rates (Talling *et al.*, 2007;
375 Jobe *et al.*, 2012). The intercalation of thin-bedded sandstones with finer-grained deposits
376 suggests a lobe fringe environment (Lobe fringe facies association, Fig. 5) (Prélat *et al.*, 2009;

Spychala *et al.*, 2017b). The abundant coarse-grained to gravelly thin-bedded sandstones in the western sector record intermittent energetic coarse-grained flows, suggesting sporadic sediment bypass processes (Stevenson *et al.*, 2015). However, the low matrix content within the granular beds suggests a sediment source area where only coarse- to granular grain size was available. The intercalation of such different facies suggests the juxtaposition of depositional environments of contrasting energy and/or different sediment sources. Either scenario could be possible given the complex sediment routing patterns and sources in a post-rift setting (e.g. (Cullen *et al.*, 2020; Hansen *et al.*, 2021), which the mass failure would exacerbate. The downdip variability in the thickness of Unit 4A (from 22 to 8.5 m thick), reduction in gravelly sandstone content and the stratigraphic thinning between the granular marker bed (red dashed line in correlation) and the top debrite (Unit 2) reveals the existence of subtle relief on the debrite surface (Fig. 3B). Furthermore, the two poorly sorted muddy sandstones, which are interpreted to be debrites, also pinch out towards the central sector. The ripples and convolute laminae with SW vergence (Fig. 3) contrast with the consistent NE paleoflow, suggesting local flow deflection (cf. Tinterri *et al.*, 2016) in the central sector, where the debrite is thickest.

Massive medium- to thick-bedded deposits of Unit 4B are interpreted as high-density turbidites formed by incremental layer-by-layer deposition with high aggradation rates (Kneller & Branney, 1995), interpreted to represent proximal lobe axis environments (lobe axis facies association; Fig. 5) (e.g. Prélat *et al.*, 2009; Kane *et al.*, 2017). The location of these facies in the westernmost sector, and the palaeoflow measurements, suggests that the western sector was relatively proximal. Banded sandstones represent the deposits of mud-rich transitional flows formed by tractional reworking (Stevenson *et al.*, 2020). The bipartite beds with a basal structureless to planar laminated sandstone division and linked mudstone clast-rich upper division are interpreted as hybrid event beds (HEBs), formed from transitional flows deposited under high-deceleration rates (Haughton *et al.*, 2009; Hodgson, 2009; Kane & Pontén, 2012)

in more distal environments than the banded sandstones (Stevenson *et al.*, 2020). The gradual and diffuse boundary between the basal turbidite and the upper debrite suggest vertical segregation of particles within the cohesive flow (Kane *et al.*, 2017). The facies evolution of Unit 4B from proximal (western sector) to distal (eastern sector) of thick-bedded sandstones into hybrid event beds likely represents the downdip transition from lobe-axis/off-axis environments (lobe axis facies association: Fig.5) (sensu Prélat *et al.*, 2009) into lobe-fringe environments (lobe fringe facies association; Fig. 5) (e.g. Kane *et al.*, 2017; Spychala *et al.*, 2017a), persisting until the frontal/oblique pinchout (e.g. Hansen *et al.*, 2019).

DEPOSITIONAL ARCHITECTURE OF THE DEBRITE AND OVERLYING UNITS

LARGE SCALE ARCHITECTURE: DEBRITE RELIEF

Using Datum A ('Burro' marker bed), the upper surface of the debrite forms a broad convex-up relief that reaches a maximum in the central section coincident with the deepest incision (at least 22.5 m of erosional relief; Fig. 3B). The spatial association of the thickest part of the debrite with the deepest incision support a genetic link between the geometry of the ramp-flat shaped basal shear zone and the mounded top. The morphology of the basal surface can buttress material translated downslope and develop positive topographic features, such as pressure ridges (Moscardelli *et al.*, 2006; Bull *et al.*, 2009). Where the upper surface of the debrite develops relief (~8 m of positive relief with respect to the western sector), it is overlain by Unit 4, and Unit 3 is absent (Fig. 3). Bed-by-bed correlation within Unit 4A, including a thin gravelly bed and tuff layer, shows a laterally continuous stratigraphic interval with metre-scale thickness variations. Unit 4A thins from 22 m (CML-1) and 13 m (CML-2) to 6 m (CML-12) across the highest part of the debrite (Fig. 3B). The lower part of Unit 4A pinches out in the central sector, developing onlaps of individual beds, and supporting the existence of a gentle relief (Bakke *et*

426 *al.*, 2013; Soutter *et al.*, 2019). In contrast, the upper part of Unit 4A shows tabular architecture
427 with a lateral continuity of over 7 km.
428 Unit 4A is overlain by Unit 4B, which shows a progressive thinning of the submarine lobe from
429 the western to the central sector over 5.6 km, from 5.7 m (CML-3) to 1.7 m (CML-12) and 1
430 m (CML-14) with a mean thinning rate of 0.9 m/km. The submarine lobe pinches out between
431 CML-14 and CML-22 (< 2 km), interfingered with unit 4A (Fig. 3B). The lack of onlap
432 geometries and thinning rates consistent with unconfined settings (e.g. Prélat *et al.*, 2009)
433 suggest a lack of pronounced relief. However, the coincidence of lobe pinch-out in the area
434 where the debrite relief is highest and where the underlying Unit 4A is thinnest might reflect
435 subtle residual relief.
436
437 *SMALL-SCALE ARCHITECTURE: FOUNDERED SANDSTONES*
438 The steeply-dipping unconformable base, internal deformation and abrupt thickness changes
439 of Unit 3 sandstones contrast with their flat and conformable tops (see stereoplots in Fig. 6).
440 These sandstone bodies can be subdivided into three different types by their architecture.
441 Type 1: The thinner foundered sandstone bodies range between 0.5- 2 m thick and are only
442 formed by the banded sandstones of the upper divisions, lacking the lower division. They are
443 characterised by 5-25 m wide lenticular shapes, with thickness/width ratios varying from 1:5
444 to 1:18. These sandstone bodies show relatively constant thinning rates (~0.25 cm/m) towards
445 their pinch outs. They are characterised by: i) advancing onlap terminations onto Unit 2 at the
446 base, indicating the interaction between the parental sediment gravity flow and debrite-related
447 relief (e.g. Bakke *et al.*, 2013), and a vertical change into; ii) progressive rotation of laminae
448 and the wedging of the sandstones, associated with syn-sedimentary loading. The juxtaposition
449 of the wedging over the onlap termination indicates that the sediment load was insufficient to

trigger the soft-sediment deformation along the upper surface at the beginning, supporting the incremental layer-by-layer deposition of these sandstones.

Type 2: Thick-bedded foundered sandstones (up to 4 m thick) are characterised by irregular stepped bases and abrupt thickness variations (up to 2 m thinning over 1 m laterally). They are composed by the juxtaposition of lower (F12 or F13) and upper divisions (F8). The lower divisions rarely exceed 10 m laterally and 3 m in thickness (thickness/width 1:2 to 2:1). In contrast, the upper divisions are more laterally extensive, with a maximum length of 50 m and rarely exceed 1 m in thickness, and thin laterally towards margins (thickness/width 1:10; Fig. 7C). The lower division shows both abrupt onlaps and wedging, indicating that the foundering began at the onset of deposition. The sediment load was enough to trigger the foundering because the debrite relief strongly influenced the initial high-concentration flows, which promoted a loss in flow capacity and deposition under high aggradation rates. The rapid deposition and foundering are responsible for the poorly-developed onlap terminations and amalgamation surfaces (Fig. 7). The deposition of lower division deposits promoted a reduction in debrite rugosity, enabling the deposition of laterally more extensive deposits. The rotation and wedging in the banding of the upper division is less well developed than in Type 1 sandstone bodies. This suggests a progressive reduction in syn-sedimentary deformation and an increase in seafloor stability (e.g. Owen, 1987, 2003). The absence of any fine-grained interval or grain-size break between the upper and lower divisions suggests continuous deposition.

Type 3: These sandstone bodies show similar facies juxtaposition as in Type 2. In this case, the sandstones terminate against heterolithic megaclasts due to their preferential location towards the top of the debrite (Fig. 7D and 7E). In these cases, the geometries of the foundered sandstones diverge from the concave-up geometry, dependent on the shape of the megaclast.

Some megaclasts disconnect bodies laterally (Fig. 4E), whereas others only impact the base, with the top part of the sandstones undisturbed (Fig. 6E).

DISCUSSION

BASAL SHEAR ZONE AND IMPACT ON THE SUBSTRATE

As submarine landslides travel across the seafloor, they exert shear stress on the substrate, coupled with significant over-pressure (Bull *et al.*, 2009; Hodgson *et al.*, 2019; Payros & Pujalte, 2019). This leads to substrate entrainment (Eggenhuisen *et al.*, 2011; Hodgson *et al.*, 2019) and/or deformation (Butler & McCaffrey, 2010; Watt *et al.*, 2012; Dakin *et al.*, 2013). The debris flow (Unit 2) incised at least 22.5 m into the substrate (Unit 1; Fig. 3). In the central sector, the basal shear surface forms ramps (up to 800 m long, >2º) and flats (up to 1550 km long; Fig 3B; between the logs CML-9 and CML-10) (see Lucente & Pini, 2003; Martinez *et al.*, 2005 for flat-ramp-flat geometry). The stress applied to the substrate during emplacement is accommodated by stratigraphic intervals (basal shear-zone) and interfaces (basal shear-surface) (Alves & Lourenço, 2010), such as the discrete basal shear zone located in upper Unit 1. The absence of contractional features in the lower stratigraphy supports the deformation being unrelated to later inversion tectonics. The basal shear zone has variable thickness and deformation styles. It is absent in the western sector, whereas erosion and deformed intervals record a high degree of basal shear stress in the central sector (Fig. 3B). In the central sector, the deformed package (up to 10 m thick) is characterised by decametre-scale thrusts with metre-scale offsets, drag folding and gravelly dykes (Fig. 4B). The predominance of imbricate thrusting over folding, and lack of internal disaggregation within the package, indicate competent substrate rheology (e.g. Van der Merwe *et al.*, 2011). The compressional regime developed when Unit 1 was consolidated enough for brittle deformation of the substrate but before its complete lithification to permit injection along rupture planes (Cobain *et al.*, 2015). The eastward vergence of the compressional structures (Fig. 4B) indicates an eastward

emplacement direction for the debris flow (Twiss & Moores, 1992), consistent with the palaeoflow indicators in the bounding strata.

The thrusting is attributed to bulldozing by the entrenched debris flow (e.g. Jackson, 2011; Hodgson *et al.*, 2019; Payros & Pujalte, 2019), representing the initial stage of substrate entrainment. Entrainment of megaclasts into a debris flow has been reported in other systems in the subsurface (Moscardelli *et al.*, 2006; Alves & Cartwright, 2009; Sawyer *et al.*, 2009; Dakin *et al.*, 2013; Ortiz-Karpf *et al.*, 2015; Soutter *et al.*, 2018; Nwoko *et al.*, 2020a) and more rarely at outcrop (Sobiesiak *et al.*, 2016; Hodgson *et al.*, 2019; Cumberpatch *et al.*, 2021). The progressive increase in thickness and degree of strain along the basal shear zone of Unit 2 and the enrichment in rafted thin-bedded megaclasts (Fig. 3B and 5) suggest downdip evolution of the debris flow, which might have affected the parental debris flow rheology (e.g. Hodgson *et al.*, 2019; Payros & Pujalte, 2019) and bulking of the flow (Gee *et al.*, 2006; Alves & Cartwright, 2009; Butler & McCaffrey, 2010; Hodgson *et al.*, 2019; Nugraha *et al.*, 2020).

DYNAMIC DEBRITE TOPOGRAPHY AND IMPACT ON OVERLYING STRATA

The absence of Unit 3 sandstones over the thickest part of the debrite suggests that the sediment gravity flows were strongly stratified and influenced by the debrite relief (Fig. 8). The sandstone bodies are also disconnected at finer scales, revealing short wavelength (metre-scale) and amplitude (decimetre-scale) rugosity on the debrite surface. The existence of simultaneous short wavelength and amplitude rugosity superimposed on a large-scale wavelength relief on the upper surface of an MTD has also been reported by Armitage *et al.* (2009), defined as 'surface-topography hierarchy', in the Cretaceous Tres Pasos Formation at the Sierra Contreras (Chile) and by Fairweather (2014) in Carboniferous Paganzo Basin at Cerro Bola (Argentina). In this study, the deposition of sand in pre-existing lows filled the short-wavelength rugosity and triggered the loading of individual sandstone bodies onto the mud-rich debrite, leaving the

524 large-scale relief underfilled. The foundering process is evidence of substrate liquefaction and
525 highlights the dynamic interface between the debrite and subsequent flows and their deposits.
526 A similar scenario was proposed by Van der Merw*e et al.* (2009, 2011) in the Vischkuil
527 Formation in the Laingsburg depocentre (Karoo Basin).

528 The ability of MTDs to pond turbidity currents travelling across their upper surface is a well-
529 known phenomenon (Kneller *et al.*, 2016). However, the presence of Unit 3 foundered
530 sandstones up-dip and down-dip of the debrite high (Fig.3B), and its consistent NE
531 paleocurrent trend, suggest connected sediment transport routes across the debrite with no
532 evidence of flow ponding or stripping (e.g. Armitage *et al.*, 2009; Fairweather, 2014). The
533 highly-stratified grown-hugging parental flows of Unit 3 would have been ponded in proximal
534 parts (western sector) if a fully enclosing topography existed given their reduced ability to
535 surmount obstacles (Al-Ja'Aidi *et al.*, 2004; Bakke *et al.*, 2013), resulting in sand starvation
536 over the debrite in distal settings (Sinclair & Tomasso, 2002; Kneller *et al.*, 2016). The
537 overlying Unit 4A can be traced laterally across the study area, with metre-scale thinning where
538 the debrite is thickest (see CML-12; Fig. 3). Apart from this, the advancing onlap geometries
539 of the thin beds and the divergence in the overall NE-orientated paleocurrents (rose diagram
540 Unit 4; Fig. 3) indicate the progressive healing of the large-scale wavelength debrite relief,
541 with some deflection of turbidity currents (Fig. 10).
542 The thin sandstone beds of the upper part of Unit 4A healed the debrite high. However, the
543 gravelly beds thin and fine from proximal to distal areas (western to eastern sectors), and the
544 two debrites pinch out in proximal areas (western sector), suggesting subtle remnant
545 topography. The different lateral continuity of individual beds is explained by different
546 rheologies of individual sediment gravity flows, which affect the flow efficiency. Cohesive
547 debris flows are more influenced by irregular relief, while low-density turbidity currents are
548 less affected by seafloor topography (Al-Ja'Aidi *et al.*, 2004; Bakke *et al.*, 2013; Soutter *et al.*,

549 2019). This suggests that laterally continuous thick accumulations of lobe fringes can develop
550 on gentle topographies, while the submarine lobes' axial parts were restricted to lower relief
551 areas. The interaction of thin-bedded turbidites successions with gentle topography has also
552 been reported in other deep-water settings (i.e., 'aggradational lobe fringes'; Spychala *et al.*,
553 2017b). The deposition of lobe fringe successions reduced confinement, which enabled the
554 deposition of the Unit 4B submarine lobe.
555 The submarine lobe is characterised by a progressive thinning and fining, developing pinch-
556 out geometries and interfingering with Unit 4A in the area where the relief of the debrite is
557 highest. The development of pinch-out geometries over the areas where the debrite shows a
558 mounded relief and where the Unit 4A onlaps and thins suggests that the relief was not wholly
559 healed with the deposition of Unit 4A and affected the parental flows of Unit 4B.
560 One explanation is that the exposure exhumes the Unit 4B lobe obliquely, with the medium- to
561 thick-bedded lobe axis deposits in the westernmost sector (CML-1 to CML-4) transitioning
562 into an HEB-dominated fringe, being highly impacted by gentle seafloor topography (Soutter
563 *et al.*, 2019; Privat *et al.*, 2021). Alternatively, the seafloor relief could have promoted the
564 modification of flow pathways and deflection of flows, thus changing the downdip orientation
565 (Fig. 8A). Another explanation is that the debrite relief in the central sector might have been
566 rejuvenated through volume changes in the debrite due to differential compaction by loading
567 the lobe itself in the proximal sector through fluid loss or fault-controlled mechanical
568 subsidence. All these scenarios suggest a confined and uncontained (see Southern *et al.*, 2015)
569 lobe-type depositional system. The precise dispersal pattern of the flows remains unknown due
570 to the outcrop limitations. Nonetheless, the documented stratigraphic evolution reveals that
571 long-lived debrite relief and progressive healing by deposition of aggradational lobe fringes
572 enabled the progradation of sand-rich submarine lobe, albeit with changes in flow rheology the
573 bed style and element-scale pinchout (Fig. 8A).

ORIGIN AND ROLE OF THE MASS-WASTING PROCESS AS TRIGGER FOR TURBIDITE SYSTEMS DEVELOPMENT

The emplacement of the large and erosional debrite in the Chacay Melehue depocentre reflects an abrupt change in sedimentation patterns, which were previously dominated by dilute mud-rich flows (Unit 1). The first significant sand influxes in the depocentre for ~6 Myr since the Aalenian (interval II of Gulisano & Gutiérrez Pleimling, 1995) are recorded by the sand-rich deposits (Unit 3) immediately overlying the debrite (Fig. 10). The juxtaposition of sand-rich turbidites over debrites (metres to hundreds of meters thick) have been reported in other systems (Kleverlaan, 1987; Labaume *et al.*, 1987; Payros *et al.*, 1999; Fallgatter *et al.*, 2017). These authors suggest that the debris flow underwent a period of mixing with ambient water, leading to the generation of an overriding co-genetic turbidity current. The foundering phenomenon reported here reveals a close spatiotemporal relationship between the debrite emplacement (Unit 2) and overlying sandstone deposition (Unit 3). To test this hypothesis, a detailed petrographic analysis is needed. An alternative mechanism is that the mass-failure event altered the basin margin physiography such that a sand source was captured. Mass-wasting processes responsible for the evacuation of material from shelf edge and upper slope areas alter the bathymetric configuration of basin margins and promote the funnelling of sediment stored in shallow marine environments through slide scars (e.g. Moscardelli & Wood, 2008; Kneller *et al.*, 2016; Steventon *et al.*, 2020; Allen *et al. in prep.*) (Fig. 11).

Given the palaeoflow and kinematic indicators, the thickness patterns of the studied units (Fig. 3B), and previous studies on sediment supply from the volcanic arc (Vicente, 2005), we propose that the mass failure originated to the west of Chacay Melehue, where a major syn-rift fault is located close to the volcanic arc (<30 km; Manceda & Figueroa, 1995; De La Cruz & Suarez, 1997; Vicente, 2005). The role of the western volcanic arc as a source area for the early

post-rift sediment supply in the Chacay Melehue depocentre is supported by the southeast directed paleocurrents measured in the Aalenian turbidite system at the base of the Los Molles Formation (Vicente, 2005; Fig. 2) and the abundance of pyroclastic deposits within Los Molles Formation stratigraphy (Zöllner & Amos, 1973; Rosenfeld & Volldaeimer, 1980; Gulisano & Gutiérrez Pleimling, 1995; De La Cruz & Suarez, 1997; Llambías & Leanza, 2005). The oyster-bearing conglomerate megaclast and well-rounded volcanic epiclast within the matrix of the debrite reflect long-lived reworking in shallow-marine settings prior to the mass failure, suggesting a shallow-water origin. This could represent the downslope transfer of sand following the collapse of volcaniclastic deposits along the magmatic arc (Fig. 8B). The evolution from the initial mass-wasting sediment supply responsible for erratically distributed foundered sandstone bodies (Unit 3) to a more mature system with the subtle distribution and diversity of lobe architectural elements (Unit 4) reflects the evolution to a more organised sediment supply system. This is abruptly superseded by a return to sand-starved conditions with dominant dilute mud-rich flows and hemipelagic deposition until the end of the Lower Callovian.

CONCLUSIONS

We document the anatomy and architecture of a kilometre-scale exhumed debrite and show how its short- and long-wavelength relief and composition provided a likely input route for the subsequent sand-rich deep-water system and influenced flow behaviour depositional patterns. The base of the debrite forms ramps and steps, indicating deep incision and entrainment of the substrate, including as megaclasts. The foundering of overlying sands, their resultant geometry and spatial distribution, and the down-dip increase in mud content, indicate a dynamic and rugose upper surface to the debrite and complex flow-deposit interactions. The spatial distribution of the foundered sandstones indicates ground-hugging flows and the existence of

debrite relief, which was progressively but not entirely healed by the submarine lobe. However, the architecture and facies distribution of the submarine lobe and their parental flows were still impacted by the long-lived, possibly rejuvenated, debrite-related topography.

The debrite emplacement coincided with an abrupt change in the stratigraphy of the Chacay Melehue depocentre from long-term mud-rich sedimentation to a transient sand-rich system. This change in depositional character is interpreted to have resulted from the funnelling of sediment stored in shallow marine environments to the west through a slide scar created by the debrite, thus reconfiguring the sediment delivery pathway.

ACKNOWLEDGEMENTS

This study is a collaboration between The University of Manchester (UK), The University of Leeds (UK), Leibniz University (Germany), The University of Liverpool (UK) and Centro de Investigaciones Geológicas (CIG) (Argentina). The authors would like to thank the local farmers of the Chacay Melehue region of Argentina for permission to carry out field studies on their land. The LOBE 3 consortium project of which this research forms a part is supported by sponsorship from Aker BP, BHP, BP, Equinor, HESS, NEPTUNE, Petrobras, PetroChina, Total, Vår Energi and Woodside, for which the authors are grateful.

FIGURES

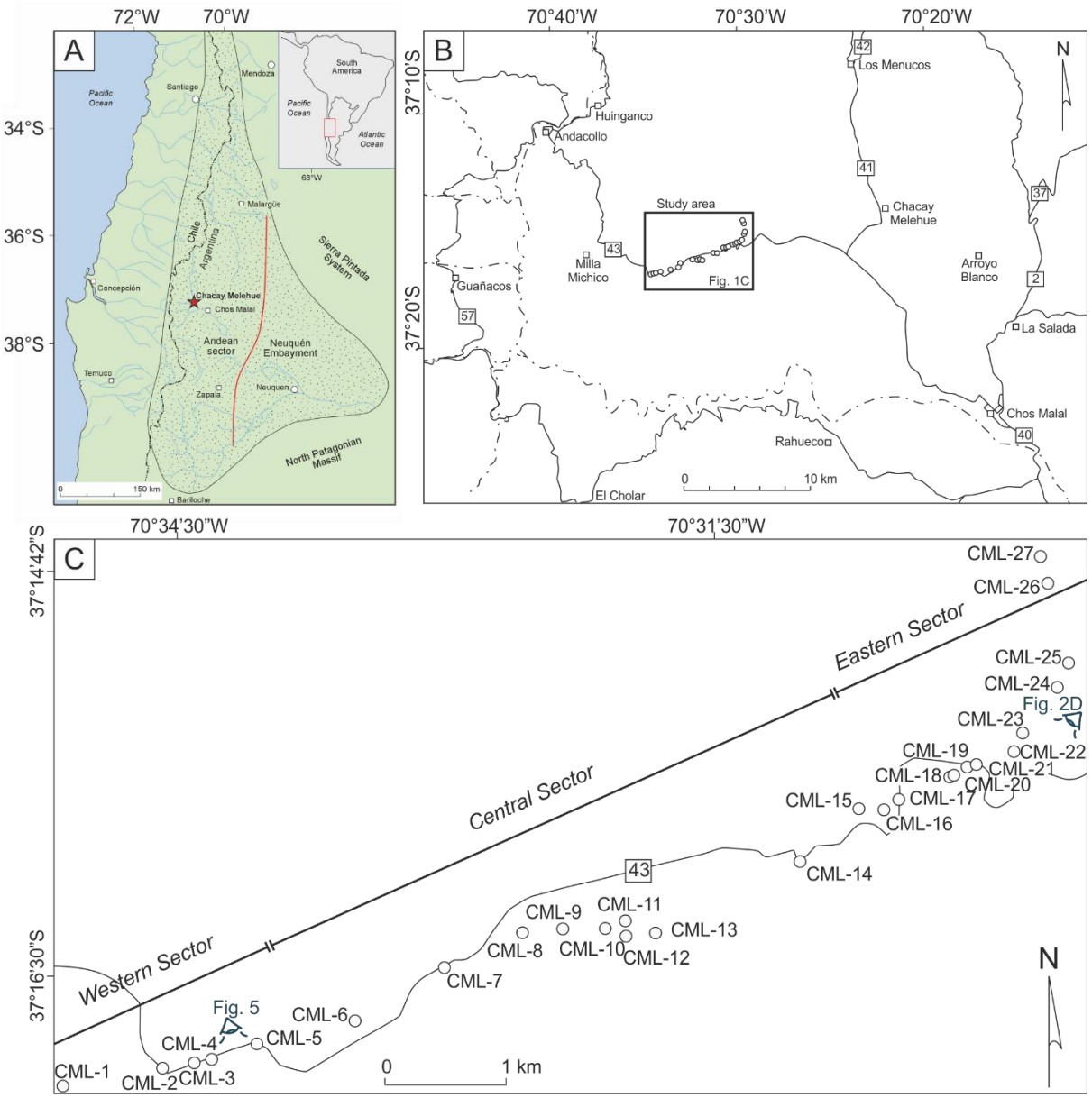

Fig. 1. (A) Location map of the Neuquén Basin and the study area Chacay Melehue (red star). (B, C) Local location map of the study area with the location of measured sections.

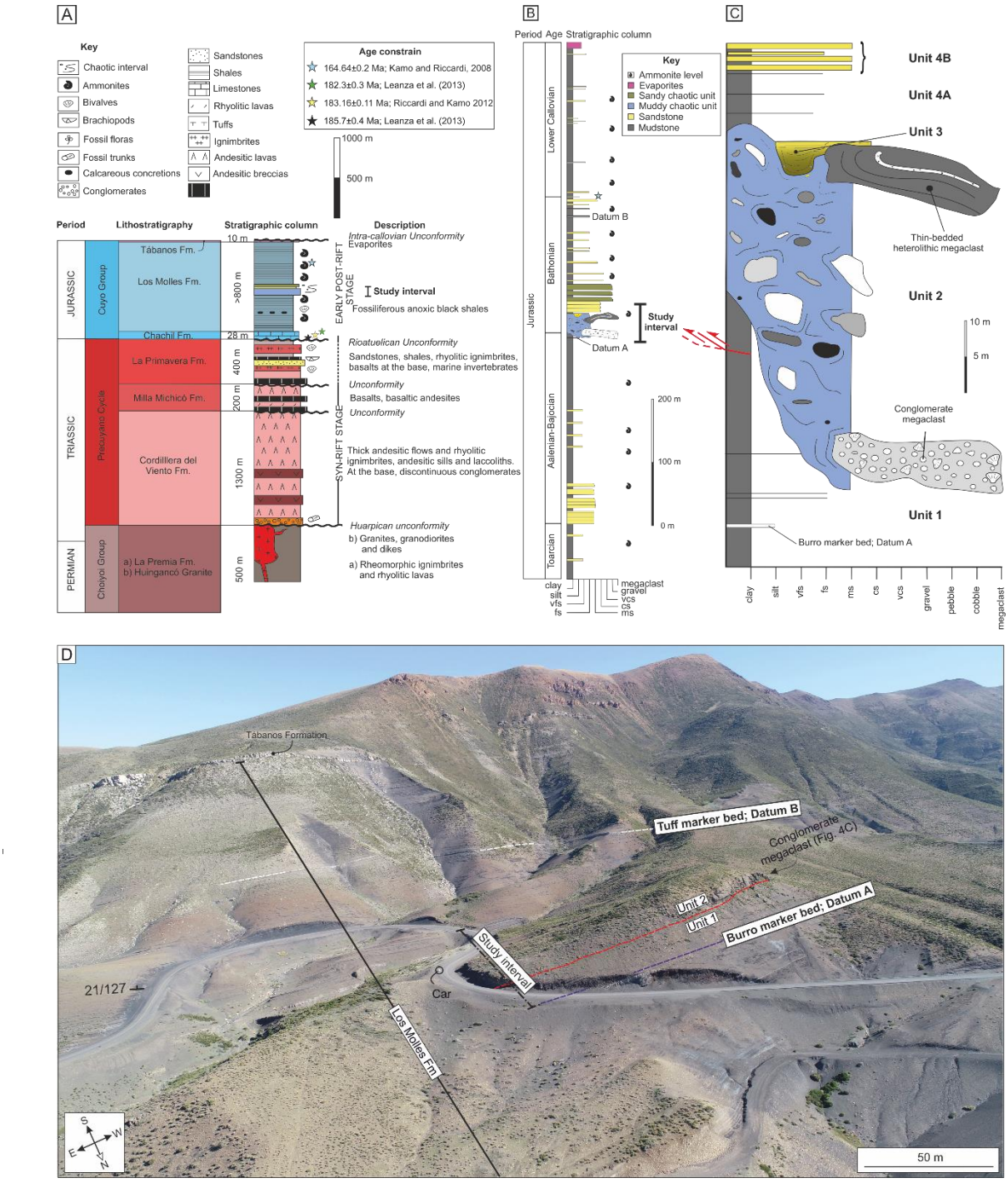

Fig. 2: (A) General stratigraphic column of Chacay Melehue showing the Los Molles Formation (modified after Gulisano and Guttiérrez-Pleimling (1995) and Llambias (2007) and Leanza et al. (2013)). (B) Stratigraphic column of Los Molles Formation and the Tábanos Formation in the Chacay Melehue area (modified after Gulisano and Guttiérrez-Pleimling (1995). (C) Schematic log of the study interval (D) Panoramic view from UAV photograph (cars on the road for scale) showing the deep-water Los Molles Formation overlain by evaporitic deposits of the Tábanos Formation. The study interval and the two datums used to constrain the base and top of the correlation panel are shown (Fig. 3A).

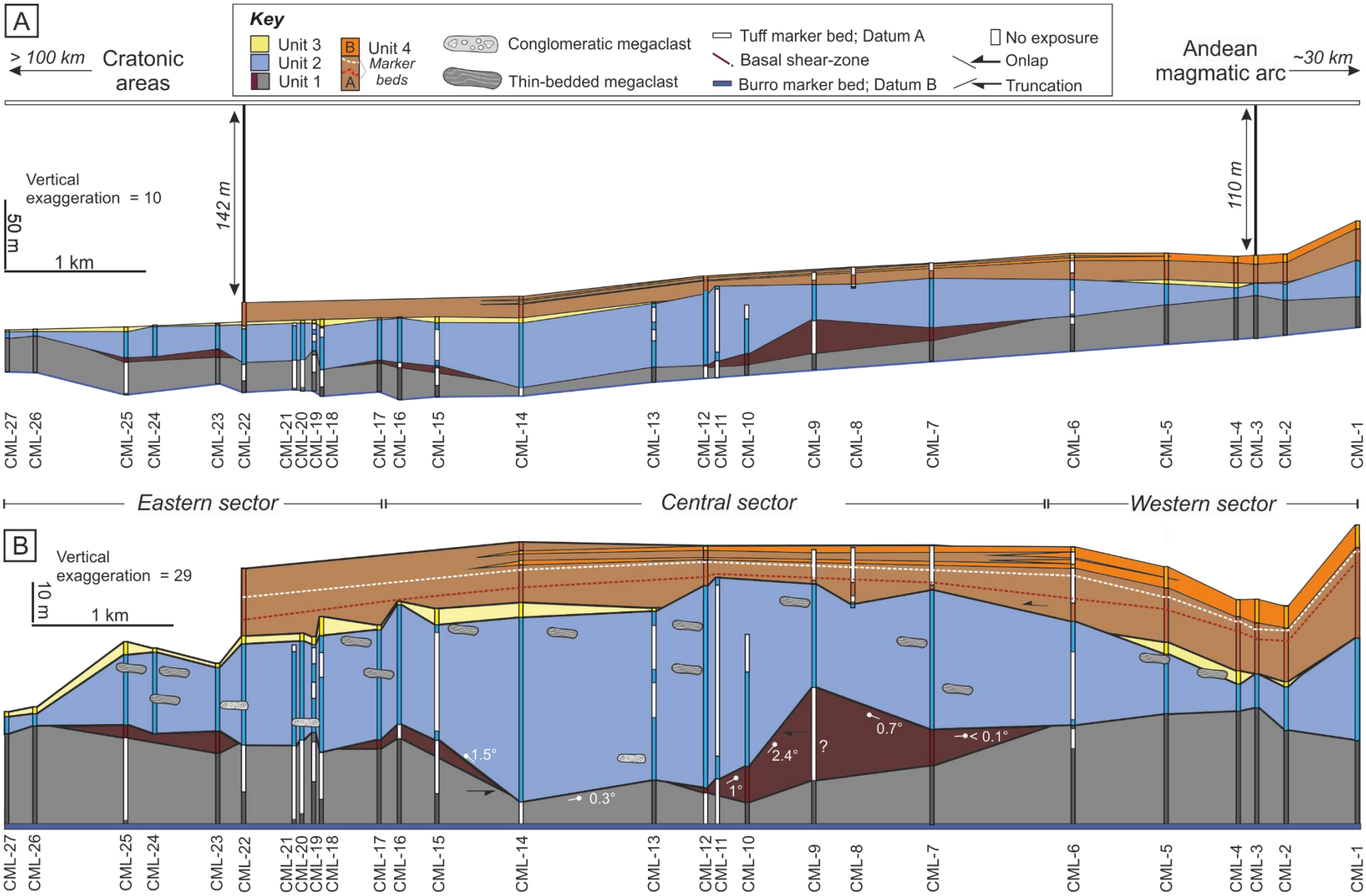
A
> 100 km
Cratonic areas
Key
Unit 3
Unit 2
Unit 1
B
A
Unit 4
Marker beds
Conglomeratic megaclast
Thin-bedded megaclast
Tuff marker bed; Datum A
Basal shear-zone
Burro marker bed; Datum B
No exposure
Onlap
Truncation
Andean magmatic arc
~30 km
Vertical exaggeration = 10
50 m
1 km
142 m
110 m
CML-27
CML-26
CML-25
CML-24
CML-23
CML-22
CML-21
CML-20
CML-19
CML-18
CML-17
CML-16
CML-15
CML-14
CML-13
CML-12
CML-11
CML-10
CML-9
CML-8
CML-7
CML-6
CML-5
CML-4
CML-3
CML-2
CML-1
Eastern sector
Central sector
Western sector
B
Vertical exaggeration = 29
10 m
1 km
1.5°
0.3°
2.4°
?
1°
0.7°
< 0.1°

Fig. 3: Correlation panels showing the spatial relationship between stratigraphic units in the Bathonian succession of the Los Molles Formation and the different depositional architectures constrained by flattening on the top and basal datums. (A) Correlation panel including Units 1 to 4 with the Tuff marker as a datum (Datum B) showing the step-like geometry of the slope. (B) Correlation panel with the basal Burro marker bed (Datum A) as a datum showing the complex ramp-flat geometry and the basal-shear zone elements (brown coloured zone) at the base of Unit 2 and the correlation within Unit 4A based on two continuous sandstone marker beds. Note the heterogeneous distribution of Unit 3 and the pinching of Unit 4B in the central sector.

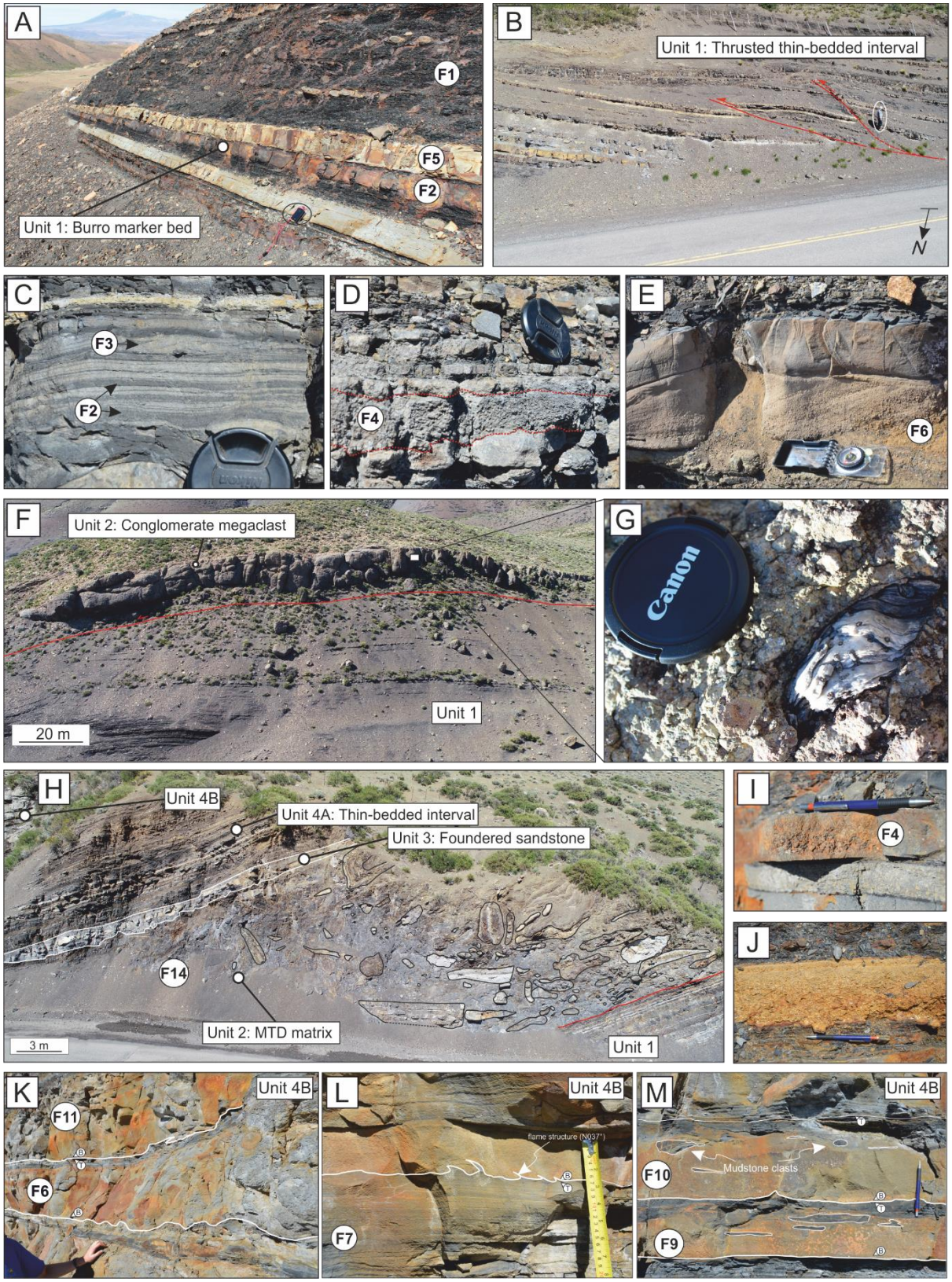
A
F1
F5
F2
Unit 1: Burro marker bed
B
Unit 1: Thrusted thin-bedded interval
N
C
F3
F2
D
F4
E
F6
F
Unit 2: Conglomerate megaclast
Unit 1
20 m
G
Canon
H
Unit 4B
Unit 4A: Thin-bedded interval
Unit 3: Foundered sandstone
F14
Unit 2: MTD matrix
Unit 1
3 m
I
F4
J
K
Unit 4B
F11
F6
L
Unit 4B
flame structure (N037°)
F7
M
Unit 4B
F10
Mudstone clasts
F9

Fig. 4: Representative sedimentary facies photos. (A) Unit 1: Planar-laminated mudstone (F1) with a few thin- to medium-bedded intercalated siltstone beds (F2) (Burro marker bed; Datum A) and sandstone beds (F5). (B) Unit 1: Basal shear-zone characterised by imbricated thrusts with drag folding. (C) Unit 4A: Heterolithic deposits consisting in the alternation between siltstones (F2) to (very) fine-grained sandstones (F3). (D) Unit 4A: Gravelly thin bed (F4) locally eroded into fine-grained sandstones (F3). (E) Unit 4A: Medium-bedded sandstones with cross-bedding (F6). (F) Unit 2: 140 m long conglomerate megaclast, bearing oyster and belemnite fragments, and sitting above Unit 1. See a fragment of an oyster in the inset (G). (H) Unit 2, 3 and 4A: Foundered sandstones onlapping the matrix-rich debrite (F14) with deformed heterolithic megaclasts draped by the thin-bedded deposits of Unit 4A. (I) Unit 4A: Gravelly and (J) Tuff-marker bed within 4A. See the correlation figure 3B and 8 (red and white dashed lines). (K) Unit 4B: Amalgamated medium- (F6) to thick-bedded (F11) sandstones. (L) Unit 4B: Medium-bedded banded sandstone (F7) overlain by massive matrix-poor sandstones (F5). Note the vergent flame structures within the amalgamation surface (M) Unit 4B: Thin- (F9) and medium-bedded (F10) hybrid event beds type 2 (cf. Haughton et al., 2009) with a linked debrite consisting of matrix-rich sandy division with elongated mudstone clasts.

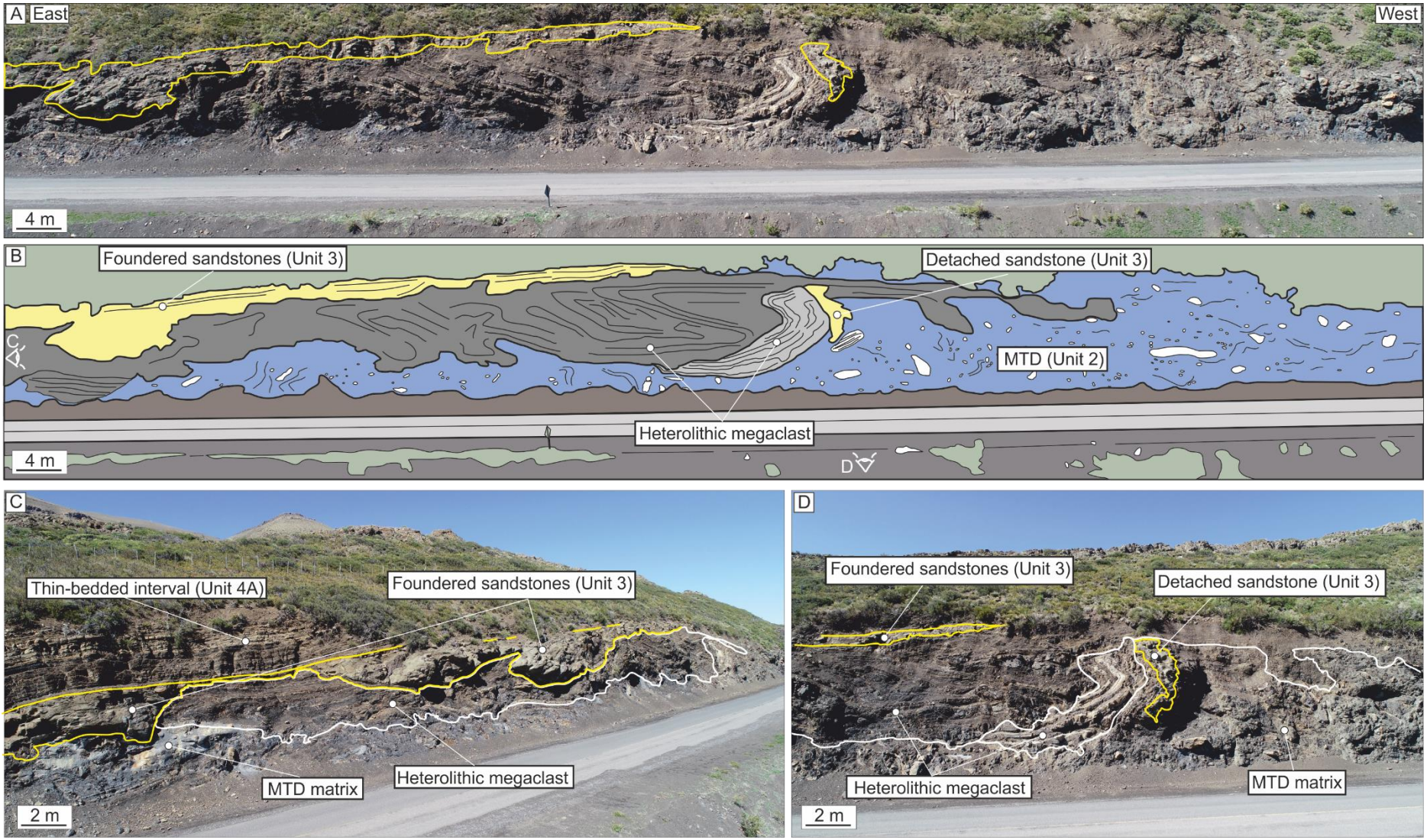

Fig. 5: (A) Panorama of the exposure. (B) Sketched exposure of A. (C) and (D) Same exposure of A from a different perspective. See B for location.

LITHOFACIES	LITHOLOGY	DESCRIPTION	THICKNESS	PROCESS INTERPRETATION
F1: Laminated mudstone.	Mudstone.	Dark-coloured planar parallel laminated mudstone with Ammonites. Concretionary horizons are common.	0.1-3 cm	Deposits from very dilute sediment gravity under relative dysoxic-anoxic conditions (Trabucho-Alexandre *et al.*, 2012; Könitzer *et al.*, 2014).
F2: Graded siltstone.	Graded siltstone.	Normally-graded from silty bases to mud-rich tops. Usually structureless, although planar parallel-laminations are common.	1-5 cm	Deposition under low-density turbidity current (Allen, 1971).
F3: Thin-bedded fine-grained sandstones.	Very fine- to fine-grained sandstones.	Normally-graded, well-sorted thin-beds. Fine-grained bases and very fine-grained tops. Structureless at the base with planar laminated tops. Rare starved ripple lamination at bed tops.	1-10 cm	Deposition and tractional reworking by low-density turbidity current (Allen, 1971, 1982; Jobe *et al.*, 2012).
F4: Thin-bedded granular sandstones.	Granular- to medium-grained sandstones.	Normally-graded, very well-sorted, coarse-grained to granular- sandstones. Sharp planar base and top.	1-10 cm	Deposition from turbidity currents.

F5: Medium-bedded sandstones.	Very fine- to medium-grained sandstone.	Structureless, normally-graded sandstones. Bed bases are medium-grained, grading-up until fine-grained.	10-50 cm	Deposition from medium-density turbidity currents. High-aggradation rates inhibited the formation of sedimentary structures (Talling et al., 2012).
F6: Thin-bedded cross-stratified sandstones.	Granular- to medium-grained sandstones.	Normally-graded, well-sorted thin-beds. Foreset heights range from 5 to 7 cm and angles vary between 10° and 35°. Erosional bases are common. Sharp contacts, with planar base and undulatory top.	5-10 cm	Deposition and tractional reworking by turbidity currents (Tinterri, 2011).
F7: Medium-bedded banded sandstones.	Banded sandstones with sharp alternation between darker and lighter bands. Lighter bands are grain-supported while darker	Sandstones comprising alternation between matrix-poor light bands and matrix-rich dark bands (0.2 to 2 cm thick). Similar grain-size (fine to medium) along with different bands. Heterolithic bedforms and pinch-and-swell geometries can be developed. The bed bases can be structureless.	10-50 cm	Deposits beneath mud-rich transitional plug flows formed by tractional reworking within the upper stage plane bed flow regime (Baas et al., 2009, 2011, 2016; Stevenson et al., 2020).

	bands are matrix-supported and lack mudstone clasts.			
F8: Thick-bedded banded sandstones with mudstone clast.	Banded sandstones with diffuse alternation between darker and lighter bands. Lighter bands are grain-supported while darker bands are matrix-supported, with abundant mudstone clasts.	Sandstones comprising banding between matrix-poor light bands and matrix-rich mudstone clast (millimetric scale) bearing dark bands (0.5-2 cm). Banding is diffuse and can be developed throughout the bed or from the middle to the top parts of a bed, commonly overlaid by convolutes lamination. Laminae shows local tilting and increasing spacing between laminae.	50-150 cm	Rapid aggradation and episodic damping of near bed turbulence due to clay flocs disagreggation (Lowe and Guy, 2000). Increasing spacing between laminae is attributed to growth strata due to foundering processes.
F9: Thin-bedded hybrid event beds.	Silty sandstone.	Matrix poor bases with linked argillaceous, ungraded and poorly-sorted top divisions.	1-10cm	Distal deposits are product of en masse deposition and potentially behaving as transitional to laminar flows (Kane *et al.*, 2017).
F10: Medium-bedded hybrid event beds.	Bipartite sandstones with matrix-poor basal divisions and upper argillaceous	Bipartite sandstone beds are characterised by a matrix-poor structureless lower division passing	10-50 cm	Deposits formed under transitional flows. Erosion and incorporation of intrabasinal clasts. The entrained substrate was rapidly disaggregated within the flow resulting in

	mudstone-clast prone division.	gradually into linked mudstone clasts matrix-rich upper division.		clast-rich and clay-rich divisions at the bed top. The flows increased in concentration but had not developed stable density stratification (Haughton *et al.*, 2003; Davis *et al.*, 2009; Hodgson, 2009; Kane & Pontén, 2012; Kane *et al.*, 2017).
F11: Thick-bedded sandstones.	Structureless sandstone.	Structureless, thick-bedded argillaceous sandstones, lacking mudstone clasts. High amalgamation rations and erosional beds when lying above fine-grained intervals. Banding is locally developed at bed tops, alternating between matrix-poor light bands and matrix-rich dark bands (0.2 to 2 cm thick). Similar grain size (fine to medium) along with different bands. Heterolithic bedforms and pinch-and-swell geometries can be developed.	0.5-1.2 m	Deposition under high-density turbidity currents (sensu Lowe, 1982), formed by incremental layer-by-layer deposition with high aggradation rates (Kneller and Branney, 1995; Sumner et al., 2008; Talling et al., 2012). The banding represent planar lamination (Bouma Tb division) (Stevenson et al., 2020).
F12: Thick-bedded structureless matrix-poor sandstones with	Structureless sandstones with a mudstone clast at the base.	Structureless thick-bedded, medium- to coarse-grained, crudely normally-graded sandstones, with low-matrix content. They contain some mudstone	0.5-2 m	Deposition under high-density turbidity currents (sensu Lowe, 1982), formed by incremental layer-by-layer deposition with

normally-graded mudstone clast.		clasts (0.1-1 m) with diffuse boundaries preferentially located at the base, which show coarse tail grading. Mudstone diapirs along the basal interface are common.		very high aggradation rates (Kneller and Branney, 1995; Sumner et al., 2008; Talling et al., 2012). Mudstone clast are entrained due to erosion of a unconsolidated debrite (Unit 2) and syn-sedimentary buoyancy product of density instabilities (Owen, 2003, 2011).
F13: Thick-bedded structureless matrix-rich sandstones with ungraded mudstone clast.	Argillaceous sandstone with abundant mudstone clasts.	Structureless thick-bedded, fine- to medium-grained, ungraded sandstones with very high matrix content and abundant decimetric mudstone clasts (0.1-1 m) randomly distributed.	0.5-2 m	Moderate-strength cohesive debris flow, derived from mudstone clast entrainment and disaggregation. Mudstone clasts are supported by their positive buoyancy with respect to the surrounding matrix and the matrix-strength (sensu Talling et al., 2012).
F14: Matrix-supported conglomerates.	Mud-rich medium-grained sandstone to sandy mudstone.	Poorly-sorted, ungraded with a chaotic distribution of outsized clasts (up to 140 m long). irregular and sharp contacts. Bases can be erosive and undulatory tops.	7.4 – 47.9 m	Cohesive debris flow deposits (Talling et al., 2012).

				with near-instantaneous deposition from a flow with high yield strength and buoyant support.

Table 1.—Descriptions of the facies recognised in the Los Molles stratigraphy of the Chacay Melehue area, including lithologies, thicknesses, and interpretations of their depositional processes.

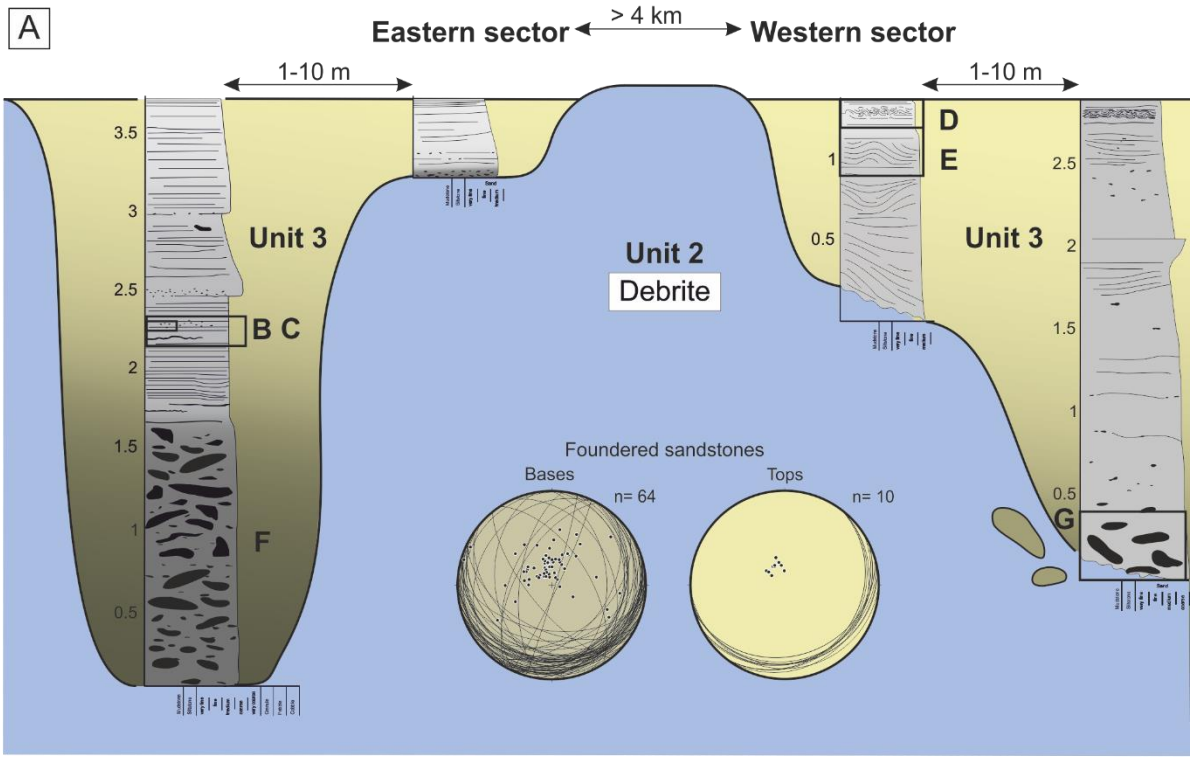
A
Eastern sector
> 4 km
Western sector
1-10 m
1-10 m
Unit 3
Unit 2
Debrite
Unit 3
B C
F
D
E
G
Foundered sandstones
Bases
n= 64
Tops
n= 10

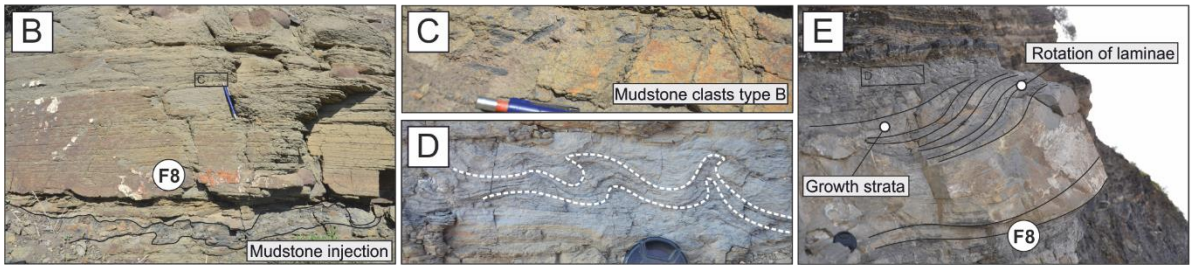
B
F8
Mudstone injection
C
Mudstone clasts type B
D
E
Rotation of laminae
Growth strata
F8

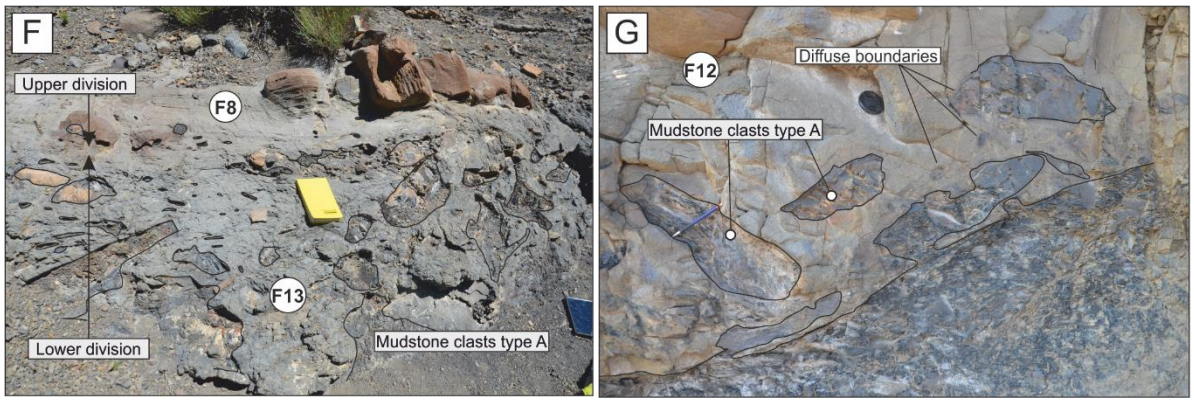
F
Upper division
F8
F13
Lower division
Mudstone clasts type A
G
F12
Diffuse boundaries
Mudstone clasts type A

Fig. 6: Foundered sandstones (Unit 3) diagram. (A) Illustrative correlation of sandstone foundering (Unit 3) into debrite (Unit 2). Note the difference between the conformable bed tops of matrix-poor and traction dominated sandstones (right-hand stereonet) and the mudstone clast- and matrix-rich sandstone texture near the unconformable bed bases (left-hand stereonet), which shows the architecture of these sandstone bodies. (B) Thick-bedded banded sandstones with bedding-parallel sill injection (F8). See mudstone clasts (type B) in the inset (C). (D) Convolute-laminae with NE vergence. (E) Sandstones showing rotation and growth strata. (F) Lower division comprising thick-bedded structureless argillaceous (F13) sandstone division with a patchy and random distribution of mudstone clasts overlain by upper division comprising thick-bedded banded sandstones (F8). (G) Thick-bedded structureless sandstone with an undulating irregular base comprising decimetre-scale mudstone clasts (type A) (F12).

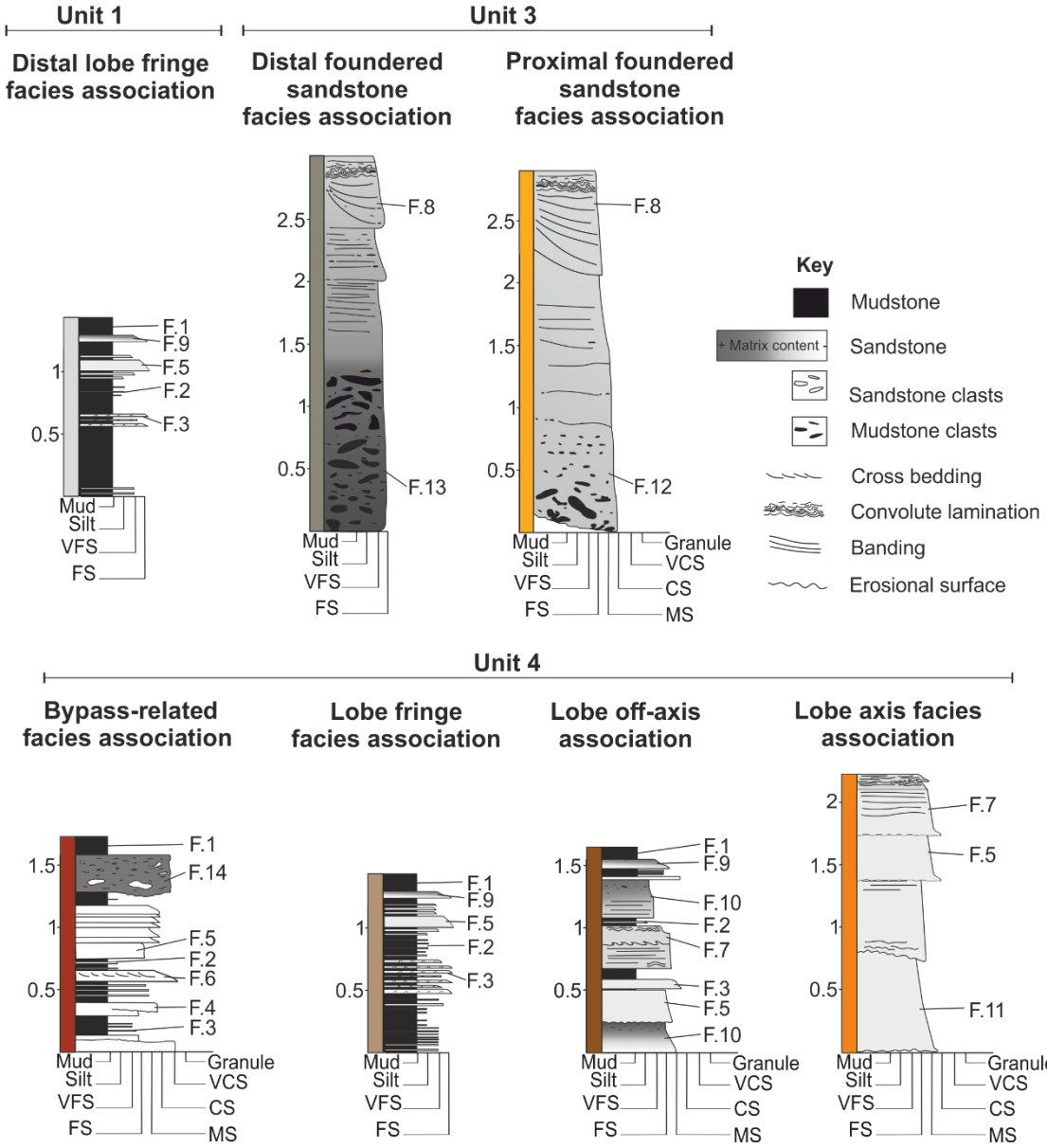
Unit 1
Unit 3
Distal lobe fringe facies association
Distal foundered sandstone facies association
Proximal foundered sandstone facies association
F.1
F.9
F.5
F.2
F.3
F.8
F.13
F.12
Mud
Silt
VFS
FS
Granule
VCS
CS
MS
Key
Mudstone
+ Matrix content -
Sandstone
Sandstone clasts
Mudstone clasts
Cross bedding
Convolute lamination
Banding
Erosional surface
Unit 4
Bypass-related facies association
Lobe fringe facies association
Lobe off-axis association
Lobe axis facies association
F.14
F.6
F.4
F.10
F.7
F.11

Fig. 7. Facies associations of Units 1, 3 and 4. See table 1 and Figs. 4 and 6 for more detail. See Fig. 8 for the lateral variability of each facies association.

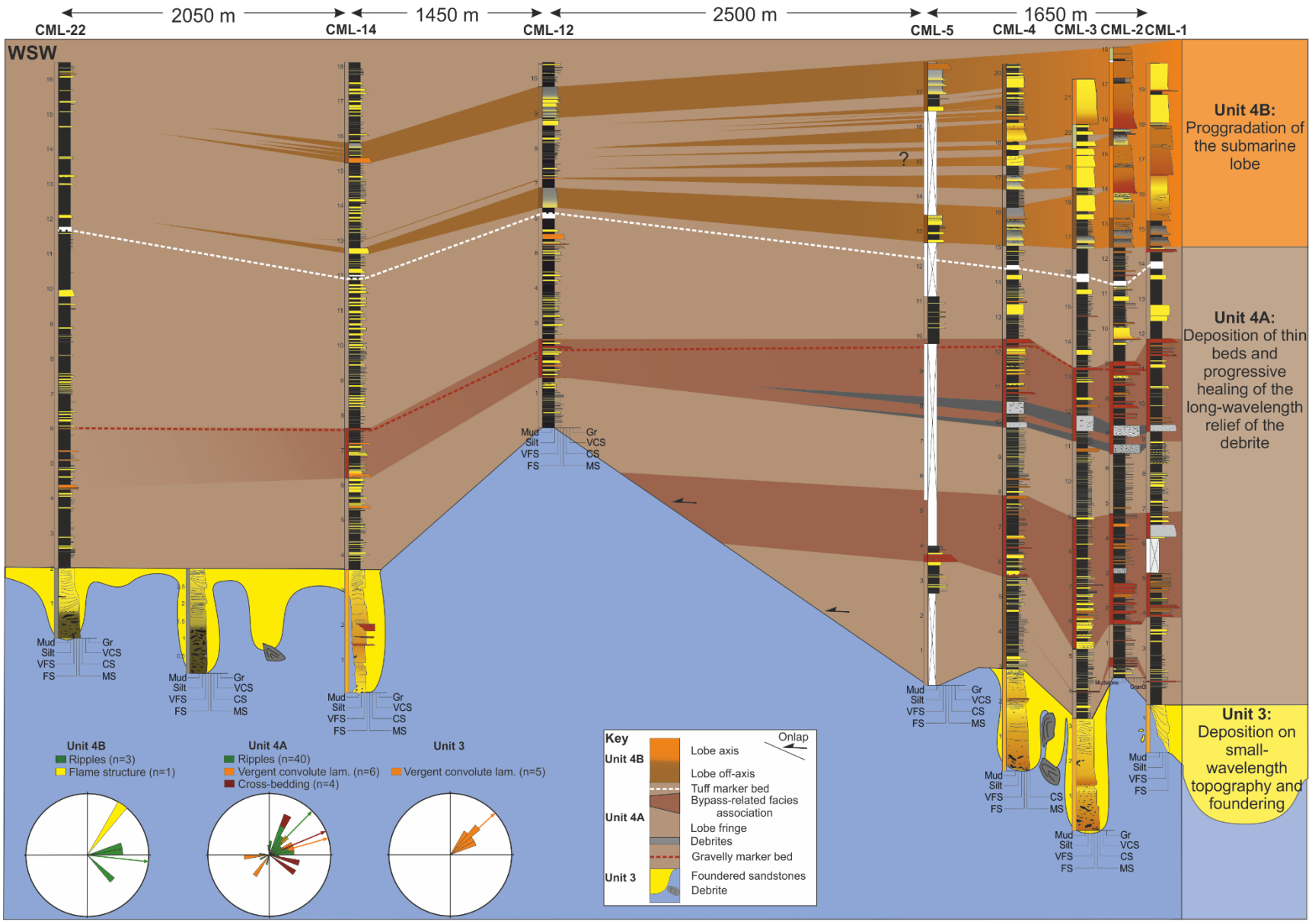
2050 m
1450 m
2500 m
1650 m
CML-22
CML-14
CML-12
CML-5
CML-4
CML-3
CML-2
CML-1
WSW
Unit 4B:
Proggradation of the submarine lobe
Unit 4A:
Deposition of thin beds and progressive healing of the long-wavelength relief of the debrite
Unit 3:
Deposition on small-wavelength topography and foundering
Mud
Silt
VFS
FS
Gr
VCS
CS
MS
Unit 4B
Ripples (n=3)
Flame structure (n=1)
Unit 4A
Ripples (n=40)
Vergent convolute lam. (n=6)
Cross-bedding (n=4)
Unit 3
Vergent convolute lam. (n=5)
Key
Onlap
Unit 4B
Lobe axis
Lobe off-axis
Tuff marker bed
Bypass-related facies association
Unit 4A
Lobe fringe
Debrites
Gravelly marker bed
Unit 3
Foundered sandstones
Debrite

Fig. 8. Correlation panel focusing on the strata (Unit 3 and 4) overlying the debrite (Unit 2). Note the colour bar next to each log representing the facies associations (see Fig. 5). Unit 3 is only present in western and eastern sectors whilst absent in the debrite high (CML-12). The lower part of Unit 4A thins and onlaps the debrite, while the upper one shows a larger lateral extent. Note the gravelly and tuff marker beds (red and white dashed lines, respectively). Unit 4A consists of alternation between fine-grained lobe fringes and coarser healing lobe fringes in the western sector. Coarse-grained healing fringes pinch out, developing fine-grained lobe fringes in the eastern sector. Unit 4B consists of amalgamated thick-bedded sandstone of lobe axis, thinning into medium-bedded dominate lobe off-axis environment in the western sector. The sand-rich lobe thins and fines towards the east, pinching out in the central sector and interfingering with the lobe fringe deposits of Unit 4A. Note that the pinch-out terminations are developed where the debrite relief is highest. The rose diagram shows the details of ripples (green), vergent convolute lamination (orange), Flame structures (yellow) and cross-bedding (red). Mean vectors of each type are shown, all suggesting a NE trend, except in Unit 4B where the ripples suggest an E-directed palaeoflow indicating deflection processes. The perimeter of the rose diagrams corresponds to 100% of the value.

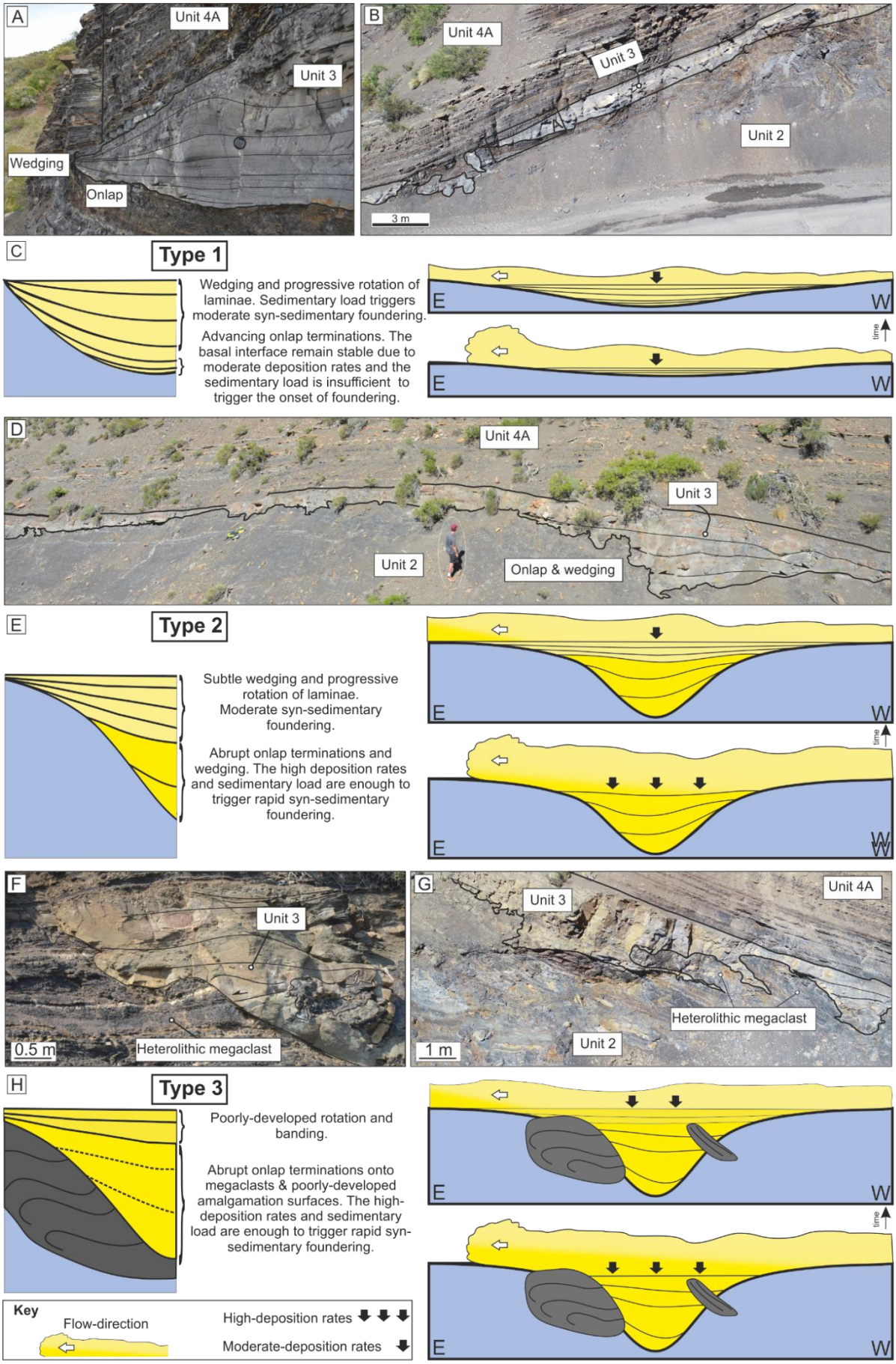
A
Unit 4A
Unit 3
Wedging
Onlap
B
Unit 4A
Unit 3
Unit 2
3 m
C
Type 1
Wedging and progressive rotation of laminae. Sedimentary load triggers moderate syn-sedimentary foundering.
Advancing onlap terminations. The basal interface remain stable due to moderate deposition rates and the sedimentary load is insufficient to trigger the onset of foundering.
E
W
time
D
Unit 4A
Unit 3
Unit 2
Onlap & wedging
E
Type 2
Subtle wedging and progressive rotation of laminae. Moderate syn-sedimentary foundering.
Abrupt onlap terminations and wedging. The high deposition rates and sedimentary load are enough to trigger rapid syn-sedimentary foundering.
F
Unit 3
0.5 m
Heterolithic megaclast
G
Unit 3
Unit 4A
Heterolithic megaclast
Unit 2
1 m
H
Type 3
Poorly-developed rotation and banding.
Abrupt onlap terminations onto megaclasts & poorly-developed amalgamation surfaces. The high-deposition rates and sedimentary load are enough to trigger rapid syn-sedimentary foundering.
Key
Flow-direction
High-deposition rates
Moderate-deposition rates

Fig. 9. Illustrative diagram of foundered sandstone architecture and a model for their development.

Type 1: (A) Thin-bedded sandstone with onlap termination at the base, indicating interaction with inherited relief and wedging associated with the syn-depositional foundering. (B) Bodies wedge smoothly, forming lenticular bodies with flat tops. Note the location of A) indicated by a black rectangle. (C) Sketch of the architecture and evolutionary model of Type 1 architecture: Initial deposition is insufficient to trigger the foundering.

Type 2: (D) Thick-bedded foundered sandstones with associated thinner margins. Central parts are composed of sandstones deposited by high-density turbidity currents, whereas the thinner margins are sandstones interpreted as being deposited under more fluidal sediment gravity flows (Transitional flows). (E) Sketch of the architecture and evolutionary model of Type 2 architecture: Initial deposition is enough to trigger the foundering.

Type 3: (F) and (G) The shape of the thick-bedded sandstone bodies depends on the size and geometry of the thin-bedded megaclast. See Fig. 5 for more detail. (H) Sketch of the architecture and evolutionary model of Type 2 architecture: While foundering, the sandstone might be protruded by the megaclast due to its higher competence than the surrounding debrite matrix.

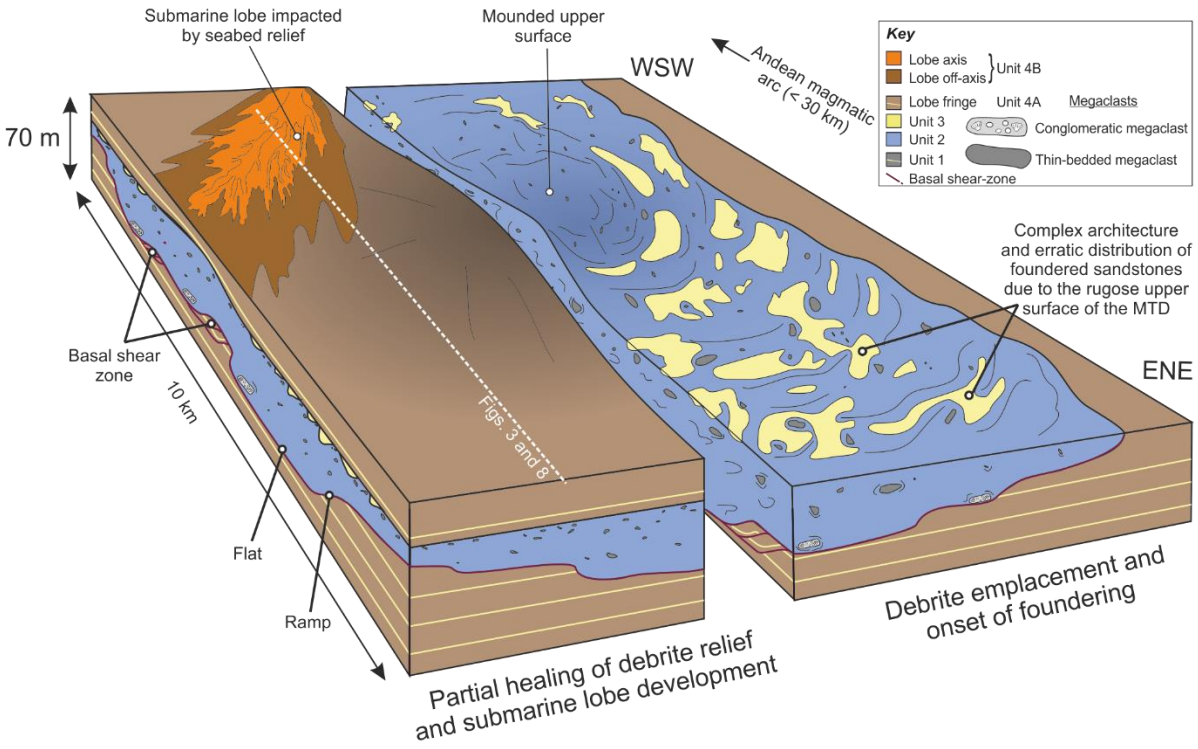

Fig. 10. Down-dip oriented schematic diagram illustrating the relief created by the debrite and the impact on younger sand-rich units. Foundered sandstones fill the small-scale rugosity, leaving the kilometre-scale accommodation underfilled. The submarine gravity flows are deflected by long-lived subtle debrite-related relief (right block). Partial healing and drapping of the debrite with the progradation od submarine lobes, which are gently impacted by the long-lived inherited relief. Note the white dashed line representing the correlation shown in Fig. 3 and 8.

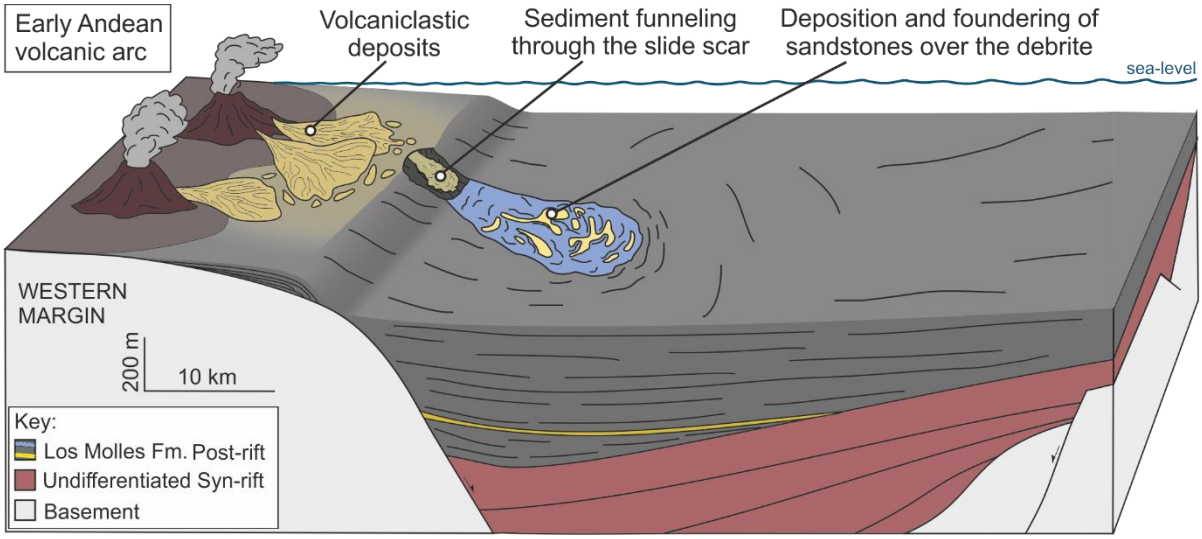

Fig. 11. (B) Schematic diagram illustrating the role of the mass failure recorded in the Chacay Melehue depocenter as the trigger for downslope remobilisation of sand from shallow-marine settings.

REFERENCES

Al-Ja'Aidi, O.S., **McCaffrey, W.D.** and **Kneller, B.C.** (2004) Factors influencing the deposit geometry of experimental turbidity currents: Implications for sand-body architecture in confined basins. *Geol. Soc. Spec. Publ.*, **222**, 45–58.

Allen, C., **Gomis-Cartesio, L.E., Hodgson, D.M., Peakall, J., and Milana, J.P.** (in press) Channel incision into a submarine landslide: an exhumed Carboniferous example from the Paganzo Basin, San Juan, Argentina 2. *The Depositional Record.*

Allen, J.R.L. (1982) Sedimentary structures, their character and physical basis Volume 1. Elsevier. 663 pp.

Alves, T.M. (2015) Submarine slide blocks and associated soft-sediment deformation in deep-water basins: A review. *Mar. Pet. Geol.*, **67**, 262–285.

Alves, T.M. and **Cartwright, J.A.** (2009) Volume balance of a submarine landslide in the Espírito Santo Basin, offshore Brazil: Quantifying seafloor erosion, sediment accumulation and depletion. *Earth Planet. Sci. Lett.*, **288**, 572–580.

Alves, T.M. and **Lourenço, S.D.N.** (2010) Geomorphologic features related to gravitational collapse: Submarine landsliding to lateral spreading on a Late Miocene-Quaternary slope (SE Crete, eastern Mediterranean). *Geomorphology*, **123**, 13–33.

Armitage, D.A., **Romans, B.W.**, **Covault, J.A.** and **Graham, S.A.** (2009) The Influence of Mass-Transport-Deposit Surface Topography on the Evolution of Turbidite Architecture: The Sierra Contreras, Tres Pasos Formation (Cretaceous), Southern Chile. *J. Sediment. Res.*, **79**, 287–301.

Baker, M.L., **Baas, J.H.**, **Malarkey, J.**, **Jacinto, R.S.**, **Craig, M.J.**, **Kane, I.A.** and **Barker, S.** (2017) The effect of clay type on the properties of cohesive sediment gravity flows and their deposits. *J. Sediment. Res.*, **87**, 1176–1195.

Bakke, K., **Kane, I.A.**, **Martinsen, O.J.**, **Petersen, S.A.**, **Johansen, T.A.**, **Hustoft, S.**, **Jacobsen, F.H.** and **Groth, A.** (2013) Seismic modeling in the analysis of deep-water sandstone termination styles. *Am. Assoc. Pet. Geol. Bull.*, **97**, 1395–1419.

Boulesteix, K., **Poyatos-Moré, M.**, **Hodgson, D.M.**, **Flint, S.S.** and **Taylor, K.G.** (2020) Fringe or background: Characterising deep-water mudstones beyond the basinfloor fan sandstone pinchout. *J. Sediment. Res.*, **90**, 1678–1705.

Brooks, H.L., **Hodgson, D.M.**, **Brunt, R.L.**, **Peakall, J.** and **Flint, S.S.** (2018) Exhumed lateral margins and increasing flow confinement of a submarine landslide complex. *Sedimentology*, **65**, 1067–1096.

Browne, G.H., **Bull, S.**, **Arnot, M.J.**, **Boyes, A.F.**, **King, P.R.** and **Helle, K.** (2020) The role of mass transport deposits contributing to fluid escape: Neogene outcrop and seismic examples from north Taranaki, New Zealand. *Geo-Marine Lett.*, **40**, 789–807.

Bull, S., **Cartwright, J.** and **Huuse, M.** (2009) A review of kinematic indicators from mass-transport complexes using 3D seismic data. *Mar. Pet. Geol.*, **26**, 1132–1151.

Butler, R.W.H., **Eggenhuisen, J.T.**, **Haughton, P.** and **McCaffrey, W.D.** (2016) Interpreting syndepositional sediment remobilisation and deformation beneath submarine gravity flows; a kinematic boundary layer approach. *J. Geol. Soc. London.*, **173**, 46–58.

Butler, R.W.H. and **McCaffrey, W.D.** (2010) Structural evolution and sediment entrainment in mass-transport complexes: Outcrop studies from Italy. *J. Geol. Soc. London.*, **167**, 617–631.

Cobain, S.L., **Peakall, J.** and **Hodgson, D.M.** (2015) Indicators of propagation direction and relative depth in clastic injectites : Implications for laminar versus turbulent flow processes. 1816–1830.

Cullen, T.M., **Collier, R.E.L.**, **Gawthorpe, R.L.**, **Hodgson, D.M.** and **Barrett, B.J.** (2020) Axial and transverse deep-water sediment supply to syn-rift fault terraces: Insights from the West Xylokastro Fault Block, Gulf of Corinth, Greece. *Basin Res.*, **32**, 1115–1149.

Dakin, N., **Pickering, K.T.**, **Mohrig, D.** and **Bayliss, N.J.** (2013) Channel-like features created by erosive submarine debris flows: Field evidence from the Middle Eocene Ainsa Basin, Spanish Pyrenees. *Mar. Pet. Geol.*, **41**, 62–71.

Damborenea, S.E. (1990) Middle Jurassic inoceramids from Argentina. *J. Paleontol.*, 736–759.

De La Cruz, R. and **Suarez, M.** (1997) El Jurásico de la cuenca de Neuquén en lonquimay, Chile: formación nacientes del biobío (38-39°S). *Rev. Geol. Chile*, **24**, 3–24.

Dykstra, M. (2005) Dynamics of Submarine Sediment Mass-Transport, from the Shelf to the Deep Sea. *PhD Thesis*, 159.

Dykstra, M., **Garyfalou, K.**, **Kertznus, V.**, **Kneller, B.C.**, **Milana, J.P.**, **Molinaro, M.**, **Szuman, M.** and **Thompson, P.** (2011) Mass-transport deposits: combining outcrop studies and seismic forward modeling to understand lithofacies distributions, deformation, and their seismic expression. In:

Posamentier, H., Weimer P. & Shipp, C. SEPM Special Publication 95, 295–310.

Eggenhuisen, J.T., **Mccaffrey, W.D.**, **Haughton, P.D.W.** and **Butler, R.W.H.** (2011) Shallow erosion beneath turbidity currents and its impact on the architectural development of turbidite sheet systems. *Sedimentology*, **58**, 936–959.

Fairweather, L. (2014) Mechanisms of supra MTD topography generation and the interaction of turbidity currents with such deposits. *PhD Thesis*, **1**, 242.

Fallgatter, C., **Kneller, B.**, **Paim, P.S.G.** and **Milana, J.P.** (2017) Transformation, partitioning and flow–deposit interactions during the run-out of megaflows. *Sedimentology*, **64**, 359–387.

Franzese, J.R. and **Spalletti, L.A.** (2001) Late triassic- Early jurassic continental extension in SouthWestern Gondwana: Tectonic segmentation and pre-break-up rifting. *J. South Am. Earth Sci.*, **14**, 257–270.

Gee, M.J.R., **Gawthorpe, R.L.** and **Friedmann, S.J.** (2006) Triggering and Evolution of a Giant Submarine Landslide, Offshore Angola, Revealed by 3D Seismic Stratigraphy and Geomorphology. *J. Sediment. Res.*, **76**, 9–19.

Gulisano, C. and **Gutiérrez Pleimling, A.R.** (1995) Field Guide. The Jurassic of the Neuquén Basin. a) Neuquén Province: Asociación Geológica Argentina. *Série E, 2*, 1–111.

Gulisano, C.A., **Gutiérrez Pleimling, A.R.** and **Digregorio, J.H.** (1984) Esquema estratigráfico de la secuencia jurásica del oeste de la provincia del Neuquén. IX Congr. Geológico Argentino 1:236–259.

Hampton, M.A., **Lee, H.J.** and **Locat., J.** (1995) Submarine Landslides. *Rev. Geophys.*, **34**, 33–59.

Hansen, L.A.S., **Hodgson, D.M.**, **Pontén, A.**, **Bell, D.** and **Flint, S.** (2019) Quantification of basin-floor fan pinchouts: Examples from the Karoo Basin, South Africa. *Front. Earth Sci.*, **7**, 1–20.

Hansen, L.A.S., **Hodgson, D.M.**, **Pontén, A.**, **Thrana, C.** and **Obradors Latre, A.** (2021) Mixed axial and transverse deep-water systems: The Cretaceous post-rift Lysing Formation, offshore Norway. *Basin Res.*, 1–23.

Haughton, P.D.W., **Davis, C.**, **McCaffrey, W.D.** and **Barker, S.P.** (2009) Hybrid sediment gravity flow deposits - Classification, origin and significance. *Mar. Pet. Geol.*, **26**, 1900–1918.

Hodgson, D.M. (2009) Distribution and origin of hybrid beds in sand-rich submarine fans of the Tanqua depocentre, Karoo Basin, South Africa. *Mar. Pet. Geol.*, **26**, 1940–1956.

Hodgson, D.M., **Brooks, H.L.**, **Ortiz-Karpf, A.**, **Spychala, Y.**, **Lee, D.R.** and **Jackson, C.A.L.** (2019) Entrainment and abrasion of megaclasts during submarine landsliding and their impact on flow behaviour. In: *G. Lintern, D.C. Mosher, L.G. Moscardelli, P.T. Bobrowsky, C. Campbell, J.D. Chaytor, J.J. Clague, A. Georgiopoulou, P. Lajeunesse, A. Normandeau, D.J.W. Piper, M. Scherwath, C. Stacey, D. Turmel, Subaqueous Mass Movements and Their Consequences*, 477, 223–240.

Howell, J.A., **Swcharz, E.**, **Spalletti, L.A.** and **Veiga, G.D.** (2005) The Neuquén Basin, Argentina: A case study in sequence stratigraphy and basin dynamics. *Geol. Soc. London, Spec. Publ.*, **252**, 1–14.

Iverson, R.M. (1997) The physics of debris flows. *Rev. Geophys.*, **35**, 245–296.

Jackson, C.A.L. (2011) Three-dimensional seismic analysis of megaclast deformation within a mass transport deposit; Implications for debris flow kinematics. *Geology*, **39**, 203–206.

Jackson, C.A.L. and **Johnson, H.D.** (2009) Sustained turbidity currents and their interaction with debrite-related topography; Labuan Island, offshore NW Borneo, Malaysia. *Sediment. Geol.*, **219**, 77–96.

Kamo, S.L. and **Riccardi, A.C.** (2009) A new U-Pb zircon age for an ash layer at the Bathonian-Callovian boundary, Argentina. *Gff*, **131**, 177–182.

Kane, I.A. and **Pontén, A.S.M.** (2012) Submarine transitional flow deposits in the Paleogene Gulf of Mexico. *Geology*, **40**, 1119–1122.

Kane, I.A., **Pontén, A.S.M.**, **Vangdal, B.**, **Eggenhuisen, J.T.**, **Hodgson, D.M.** and **Spychala, Y.T.** (2017) The stratigraphic record and processes of turbidity current transformation across deep-marine lobes. *Sedimentology*, **64**, 1236–1273.

Kleverlaan, K. (1987) Gordo megabed: a possible seismite in a tortonian submarine fan, tabernas basin, province almeria, southeast spain. *Sediment. Geol.*, **51**, 165–180.

Kneller, B., **Dykstra, M.**, **Fairweather, L.** and **Milana, J.P.** (2016) Mass-transport and slope accommodation: implications for turbidite sandstone reservoirs. *Am. Assoc. Pet. Geol. Bull.*, **100**, 213–235.

Kneller, B.C. and **Branney, M.J.** (1995) Sustained high-density turbidity currents and the deposition of thick massive sands. *Sedimentology*, **42**, 607–616.

Könitzer, S.F., **Davies, S.J.**, **Stephenson, M.H.** and **Leng, M.J.** (2014) Depositional controls on

mudstone lithofacies in a basinal setting: Implications for the delivery of sedimentary organic matter. *J. Sediment. Res.*, **84**, 198–214.

Labaume, P., **Mutti, E.** and **Seguret, M.** (1987) Megaturbidites : A Depositional Model From the Eocene. *Geo-Marine Lett.*, **7**, 91–101.

Leanza, H.A., **Mazzini, A.**, **Corfu, F.**, **Llambías, E.J.**, **Svensen, H.**, **Planke, S.** and **Galland, O.** (2013) The Chachil Limestone (Pliensbachian-earliest Toarcian) Neuquén Basin, Argentina: U-Pb age calibration and its significance on the Early Jurassic evolution of southwestern Gondwana. *J. South Am. Earth Sci.*, **42**, 171–185.

Lee, C., **Nott, J.A.**, **Keller, F.B.** and **Parrish, A.R.** (2004) Seismic expression of the cenozoic mass transport complexes deep-water Tarfaya-Agadir Basin offshore Morocco. *Proc. Annu. Offshore Technol. Conf.*, **3**, 1891–1908.

Legarreta, L. and **Gulisano, C.A.** (1989) Análisis estratigráfico secuencial de la Cuenca Neuquina (Triásico superior-Terciario inferior). In: *Cuencas sedimentarias argentinas.*, 221–243.

Legarreta, L. and **Uliana, M.A.** (1996) The Jurassic succession in west-central Argentina: Stratal patterns, sequences and paleogeographic evolution. *Palaeogeogr. Palaeoclimatol. Palaeoecol.*, **120**, 303–330.

Llambías, E.J. and **Leanza, H.A.** (2005) Depósitos laháricos en la formación los molles en chacay melehue, neuquén: Evidencia de volcanismo jurásico en la cuenca neuquina. *Rev. la Asoc. Geol. Argentina*, **60**, 552–558.

Llambías, E.J., **Leanza, H.A.** and **Carbone, O.** (2007) Evolución Tectono-magmática durante el pérmico al Jurásico temprano en la Cordillera del Viento (37°05'S - 37°15'S): Nuevas evidencias geológicas y geoquímicas Del Inicio de la Cuencas Neuquina. *Rev. la Asoc. Geol. Argentina*, **62**, 217–235.

Llambías, E.J., **Quenardelle, S.** and **Montenegro, T.** (2003) The Choiyoi Group from central Argentina: A subalkaline transitionalto alkaline association in the craton adjacent to the active marginof the Gondwana continent. *J. South Am. Earth Sci.*, **16**, 243–257.

Lowe, D.R. (1982) Sediment gravity flows; II, Depositional models with special reference to the deposits of high-density turbidity currents. *J. Sediment. Res.*, **52**, 279–297.

Lowe, D.R. and **Guy, M.** (2000) Slurry-flow deposits in the Britannia Formation (Lower Cretaceous), North Sea: A new perspective on the turbidity current and debris flow problem. *Sedimentology*, **47**, 31–70.

Lucente, C.C. and **Pini, G.A.** (2003) Anatomy and emplacement mechanism of a large submarine slide within a miocene foredeep in the Northern Apennines, Italy: A field perspective. *Am. J. Sci.*, **303**, 565–602.

Major, J.J. and **Iverson, R.M.** (1999) Debris-flow deposition: Effects of pore-fluid pressure and friction concentrated at flow margins. *Bull. Geol. Soc. Am.*, **111**, 1424–1434.

Manceda, R. and **Figueroa, D.** (1995) Inversion of the Mesozoic Neuquen Rift in the Malargue fold and thrust belt, Mendoza, Argentina. *Pet. basins South Am.*, **62**, 369–382.

Martinez, J.F., **Cartwright, J.** and **Hall, B.** (2005) 3D seismic interpretation of slump complexes: Examples from the continental margin of Israel. *Basin Res.*, **17**, 83–108.

McClelland, H.L.O., **Woodcock, N.H.** and **Gladstone, C.** (2011) Eye and sheath folds in turbidite convolute lamination: Aberystwyth Grits Group, Wales. *J. Struct. Geol.*, **33**, 1140–1147.

McGilvery, T.A. and **Cook, D.L.** (2003) The Influence of Local Gradients on Accommodation Space and Linked Depositional Elements Across a Stepped Slope Profile, Offshore Brunei. Shelf Margin Deltas Linked Down Slope Pet. Syst. 23rd Annu. 387–419.

Migeon, S., **Ceramicola, S.**, **Praeg, D.**, **Ducassou, E.**, **Dano, A.**, **Ketzer, J.M.**, **Mary, F.** and **Mascle, J.** (2014) Post-failure Processes on the Continental Slope of the Central Nile Deep-Sea Fan: Interactions Between Fluid Seepage, Sediment Deformation and Sediment-Wave Construction. In: *Submarine Mass Movements and Their Consequences. Advances in Natural and Technological Hazards Research, vol 37. Springer, Cham. https://doi.org/10.1007/978-3-319-00972-8_11*, 201–212.

Moscardelli, L. and **Wood, L.** (2008) New classification system for mass transport complexes in offshoreTrinidad. 73–98.

Moscardelli, L., **Wood, L.** and **Mann, P.** (2006) Mass-transport complexes and associated processes in the offshore area of Trinidad and Venezuela. *Am. Assoc. Pet. Geol. Bull.*, **90**, 1059–1088.

Mulder, T. and **Alexander, J.** (2001) The physical character of subaqueous sedimentary density flows and their deposits. *Sedimentology*, **48**, 269–299.

Mutti, E. (1977) Distinctive thin-bedded turbidite facies and related depositional environments in the Eocene Hecho Group (South-central Pyrenees, Spain). *Sedimentology*, **24**, 107–131.

Nardin, T.R., **Hein, F.J.**, **Gorsline, D.S.** and **Edwards, B.D.** (1979) A review of mass movement processes

sediment and acoustic characteristics, and contrasts in slope and base-of-slope systems versus canyon-fan-basin floor systems. *SEPM Spec. Publ.*, **27**, 61–73.

Nugraha, H.D., **Jackson, C.A.L.**, **Johnson, H.D.**, **Hodgson, D.M.** and **Clare, M.** (2020) How erosive are submarine landslides? Eartharxiv. doi: https://doi.org/10.31223/osf.io/cpx9e

Nwoko, J., **Kane, I.** and **Huuse, M.** (2020a) Megaclasts within mass-transport deposits: Their origin, characteristics and effect on substrates and succeeding flows. *Geol. Soc. Spec. Publ.*, **500**, 515–530.

Nwoko, J., **Kane, I.** and **Huuse, M.** (2020b) Mass transport deposit (MTD) relief as a control on post-MTD sedimentation: Insights from the Taranaki Basin, offshore New Zealand. *Mar. Pet. Geol.*, **120**, 104489.

Ortiz-Karpf, A., **Hodgson, D.M.**, **Jackson, C.A.-L.** and **McCaffrey, W.D.** (2017) Influence of Seabed Morphology and Substrate Composition On Mass-Transport Flow Processes and Pathways: Insights From the Magdalena Fan, Offshore Colombia. *J. Sediment. Res.*, **87**, 189–209.

Ortiz-Karpf, A., **Hodgson, D.M.** and **McCaffrey, W.D.** (2015) The role of mass-transport complexes in controlling channel avulsion and the subsequent sediment dispersal patterns on an active margin: The Magdalena Fan, offshore Colombia. *Mar. Pet. Geol.*, **64**, 58–75.

Owen, G. (1987) Deformation processes in unconsolidated sands. *Geol. Soc. Spec. Publ.*, **29**, 11–24.

Owen, G. (2003) Load structures: Gravity-driven sediment mobilisation in the shallow subsurface. *Geol. Soc. Spec. Publ.*, **216**, 21–34.

Pángaro, F., **Pereira, D.M.** and **Micucci, E.** (2009) El sinrift de la dorsal de Huincul, Cuenca Neuquina: Evolución y control sobre la estratigrafía y estructura del área. *Rev. la Asoc. Geol. Argentina*, **65**, 265–277.

Payros, A. and **Pujalte, V.** (2019) Eocene Mass-Transport Deposits in the Basque Basin (Western Pyrenees, Spain). 155–170.

Payros, A., **Pujalte, V.** and **Orue-Etxebarria, X.** (1999) The South Pyrenean Eocene carbonate megabreccias revisited: New interpretation based on evidence from the Pamplona Basin. *Sediment. Geol.*, **125**, 165–194.

Pickering, K.T. and **Corregidor, J.** (2005) Mass-transport complexes (MTCs) and tectonic control on basin-floor submarine fans, middle Eocene, South Spanish Pyrenees. *J. Sediment. Res.*, **75**, 761–

783.

Praeg, D., **Ketzer, J.M.**, **Adolpho Herbert, A.**, **Migeon, S.**, **Ceramicola, S.**, **Alexandre, D.**, **Emmanuelle, Ducassou Stéphanie, D.**, **Jean, M.** and **Rodrigues, L.F.** (2014) Fluid seepage in relation to seabed deformation on the central Nile deep-sea fan, part 2: evidence from multibeam and sidescan imagery. In: *Submarine Mass Movements and Their Consequences. Advances in Natural and Technological Hazards Research. 6th International Symposium. Volume 37.https://doi.org/10.1007/978-3-319-00972-8_11*, 37, 141–150.

Prélat, A., **Hodgson, D.M.** and **Flint, S.S.** (2009) Evolution, architecture and hierarchy of distributary deep-water deposits: a high-resolution outcrop investigation from the Permian Karoo Basin, South Africa. *Sedimentology*, **56**, 2132–2154.

Privat, A.M.J., **Hodgson, D.M.**, **Jackson, C.A.L.**, **Schwarz, E.** and **Peakall, J.** (2021) Evolution from syn-rift carbonates to early post-rift deep-marine intraslope lobes: The role of rift basin physiography on sedimentation patterns. *Sedimentology*, 0–2.

Riccardi, A. and **Kamo, S.** (2014) Biostratigraphy and Geochronology of the Pliensbachian-Toarcian Boundary in Argentina. *XIX Congr. Geológico Argentino, Junio 2014, Córdoba*, **Actas T1**-**4**, 9–11.

Riccardi, A.C. (2008) The marine Jurassic of Argentina: A biostratigraphic framework. *Episodes*, **31**, 326–335.

Riccardi, A.C., **Damborenea, S.E.**, **Manceñido, M.O.** and **Leanza, H.A.** (2011) Megainvertebrados del Jurásico y su importancia geobiológica. *Relat. del XVIII Congr. Geológico Argentino, Neuquén*, 441–464.

Rosenfeld, U. and **Volldaeimer, W.** (1980) Turbidite und andere Rhythmite im tieferen Jura des Neuquén-Beckens (Argentinien). 379–421.

Sawyer, D.E., **Flemings, P.B.**, **Dugan, B.** and **Germaine, J.T.** (2009) Retrogressive failures recorded in mass transport deposits in the Ursa Basin, Northern Gulf of Mexico. *J. Geophys. Res. Solid Earth*, **114**, 1–20.

Sinclair, H.D. and **Tomasso, M.** (2002) Depositional Evolution of Confined Turbidite Basins. *J. Sediment. Res.*, **72**, 451–456.

Sobiesiak, M.S., **Kneller, B.**, **Alsop, G.I.** and **Milana, J.P.** (2016) Internal deformation and kinematic indicators within a tripartite mass transport deposit, NW Argentina. *Sediment. Geol.*, **344**, 364–381.

Southern, S.J., **Patacci, M.**, **Felletti, F.** and **McCaffrey, W.D.** (2015) Influence of flow containment and substrate entrainment upon sandy hybrid event beds containing a co-genetic mud-clast-rich division. *Sediment. Geol.*, **321**, 105–122.

Soutter, E., Kane, I.A., and Huuse, M. (2018). Giant submarine landslide triggered by Paleocene mantle plume activity in the North Atlantic. Geology, **46**, 511-514.

Soutter, E.L., **Kane, I.A.**, **Fuhrmann, A.**, **Cumberpatch, Z.A.** and **Huuse, M.** (2019) The stratigraphic evolution of onlap in siliciclastic deep-water systems: Autogenic modulation of allogenic signals. *J. Sediment. Res.*, **89**, 890–917.

Spalletti, L.A., **Parent, H.**, **Veiga, G.D.** and **Schwarz, E.** (2012) Amonites y bioestratigrafía del Grupo Cuyo en la Sierra de Reyes (cuenca Neuquina central, Argentina) y su significado secuencial. *Andean Geol.*, **39**, 464–481.

Spychala, Y.T., **Hodgson, D.M.**, **Prélat, A.**, **Kane, I.A.**, **Flint, S.S.** and **Mountney, N.P.** (2017a) Frontal and lateral submarine lobe fringes: Comparing sedimentary facies, architecture and flow processes. *J. Sediment. Res.*, **87**, 75–96.

Spychala, Y.T., **Hodgson, D.M.**, **Stevenson, C.J.** and **Flint, S.S.** (2017b) Aggradational lobe fringes: The influence of subtle intrabasinal seabed topography on sediment gravity flow processes and lobe stacking patterns. *Sedimentology*, **64**, 582–608.

Stevenson, C.J., **Jackson, C.A.L.**, **Hodgson, D.M.**, **Hubbard, S.M.** and **Eggenhuisen, J.T.** (2015) Deep-water sediment bypass. *J. Sediment. Res.*, **85**, 1058–1081.

Stevenson, C.J., **Peakall, J.**, **Hodgson, D.M.**, **Bell, D.** and **Privat, A.** (2020) Tb or not Tb: Banding in Turbidite Sandstones.

Steventon, M.J., **Jackson, C.A.**, **Johnson, H.D.** and **Hodgson, D.M.** (2021) Evolution of a sand-rich submarine channel–lobe system, and the impact of mass-transport and transitional-flow deposits on reservoir heterogeneity: Magnus Field, Northern North Sea.

Steventon, M.J., **Jackson, C.A.L.**, **Hodgson, D.M.** and **Johnson, H.D.** (2020) Lateral variability of shelf-edge and basin-floor deposits, Santos Basin, Offshore Brazil. *J. Sediment. Res.*, **90**, 1198–1221.

Stow, D.A.V. and **Johansson, M.** (2000) Deep-water massive sands: Nature, origin and hydrocarbon implications. *Mar. Pet. Geol.*, **17**, 145–174.

Suárez, M. and **de la Cruz, R.** (1997) Volcanismo pliniano del Lías durante los inicios de la cuenca de

Neuquén, Cordillera del Viento, Neuquén, Argentina. Actas 7º Congr. Geológico Chil. 266–270.

Sumner, E.J., **Amy, L.A.** and **Talling, P.J.** (2008) Deposit structure and processes of sand deposition from decelerating sediment suspensions. *J. Sediment. Res.*, **78**, 529–547.

Talling, P.J., **Masson, D.G.**, **Sumner, E.J.** and **Malgesini, G.** (2012) Subaqueous sediment density flows: Depositional processes and deposit types. *Sedimentology*, **59**, 1937–2003.

Tinterri, R., **Muzzi Magalhaes, P.**, **Tagliaferri, A.** and **Cunha, R.S.** (2016) Convolute laminations and load structures in turbidites as indicators of flow reflections and decelerations against bounding slopes. Examples from the Marnoso-arenacea Formation (northern Italy) and Annot Sandstones (south eastern France). *Sediment. Geol.*, **344**, 382–407.

Trabucho-Alexandre, J., **Dirkx, R.**, **Veld, H.**, **Klaver, G.** and **De Boer, P.L.** (2012) Toarcian black shales in the dutch central graben: Record of energetic, variable depositional conditions during an oceanic anoxic event. *J. Sediment. Res.*, **82**, 104–120.

Twiss, R.J. and **Moores, E.M.** (1992) Structural Geology. W.H. Freeman and Company, New York.

Valdez, V., **Milana, J.P.**, **Sobiesiak, M.S.** and **Kneller, B.** (2019) The Carboniferous MTD Complex at La Peña Canyon, Paganzo Basin (San Juan, Argentina). 105–116.

Van der Merwe, W.C., **Hodgson, D.M.** and **Flint, S.S.** (2009) Widespread syn-sedimentary deformation on a muddy deep-water basin-floor: The vischkuil formation (Permian), Karoo Basin, South Africa. *Basin Res.*, **21**, 389–406.

Van der Merwe, W.C., **Hodgson, D.M.** and **Flint, S.S.** (2011) Origin and terminal architecture of a submarine slide: A case study from the Permian Vischkuil Formation, Karoo Basin, South Africa. *Sedimentology*, **58**, 2012–2038.

Veiga, G.D., **Schwarz, E.** and **Spalletti, L.A.** (2011) Análisis estratigráfico de la Formación Lotena (Calloviano superior- Oxfordiano inferior) en la Cuenca Neuquina Central, República Argentina. Integración de información de afloramientos y subsuelo. *Andean Geol.*, **38**, 171–197.

Veiga, G.D., **Schwarz, E.**, **Spalletti, L.A.** and **Massaferro, J.L.** (2013) Anatomy And Sequence Architecture of the Early Post-Rift In the Neuquen Basin (Argentina): A Response To Physiography and Relative Sea-Level Changes. *J. Sediment. Res.*, **83**, 746–765.

Vergani, G.D., **Tankard, A.J.**, **Belotti, H.J.** and **Welsink, H.J.** (1995) Tectonic Evolution and Paleogeography of the Neuquén Basin, Argentina. *Pet. basins South Am.*, **1904**, 383–402.

Vicente, J.C. (2005) Dynamic paleogeography of the Jurassic Andean Basin: Pattern of transgression and localisation of main straits through the magmatic arc. *Rev. la Asoc. Geol. Argentina*, **60**, 221–250.

Watt, S.F.L., **Talling, P.J.**, **Vardy, M.E.**, **Masson, D.G.**, **Henstock, T.J.**, **Hühnerbach, V.**, **Minshull, T.A.**, **Urlaub, M.**, **Lebas, E.**, **Le Friant, A.**, **Berndt, C.**, **Crutchley, G.J.** and **Karstens, J.** (2012) Widespread and progressive seafloor-sediment failure following volcanic debris avalanche emplacement: Landslide dynamics and timing offshore Montserrat, Lesser Antilles. *Mar. Geol.*, **323**–**325**, 69–94.

Weaver, C. (1931) Paleontology of the Jurassic and Cretaceous of West Central Argentina. Memoir University of Washington 1.

Weaver, C. (1942) A general summary of the Mesozoic of South and Central America. In: *Proceedings of the eighth American scientific congress held in Washington May 10-18*, 149–193.

Zöllner, W. and **Amos, A.J.** (1973) Descripción geológica de la hoja 32b, Chos Malal. Servicio Geológico Nacional. 97 pp.